PARAMETER ESTIMATION OF MULTICOMPONENT MICRO-DOPPLER SIGNALS

A THESIS SUBMITTED TO
THE GRADUATE SCHOOL OF NATURAL AND APPLIED SCIENCES
OF
MIDDLE EAST TECHNICAL UNIVERSITY

BY

HÜSEYİN YILDIZ

IN PARTIAL FULFILLMENT OF THE REQUIREMENTS
FOR
THE DEGREE OF MASTER OF SCIENCE
IN
ELECTRICAL AND ELECTRONICS ENGINEERING

JUNE 2014

Approval of the thesis:

PARAMETER ESTIMATION OF MULTICOMPONENT MICRO-DOPPLER SIGNALS

submitted by **HÜSEYİN YILDIZ** in partial fulfillment of the requirements for the degree of **Master of Science in Electrical and Electronics Engineering Department, Middle East Technical University** by,

Prof. Dr. Canan Özgen
Dean, Graduate School of **Natural and Applied Sciences** _____

Prof. Dr. Gönül Turhan Sayan
Head of Department, **Electrical and Electronics Engineering** _____

Prof. Dr. Mete Severcan
Supervisor, **Electrical and Electronics Eng. Dept., METU** _____

Examining Committee Members:

Prof. Dr. Yalçın Tanık
Electrical and Electronics Engineering Dept., METU _____

Prof. Dr. Mete Severcan
Electrical and Electronics Engineering Dept., METU _____

Prof. Dr. Sencer Koç
Electrical and Electronics Engineering Dept., METU _____

Assoc. Prof. Dr. Çağatay Candan
Electrical and Electronics Engineering Dept., METU _____

Özgür İnce, M.Sc.
Senior Researcher, ILTAREN BILGEM TÜBITAK _____

Date: _____

I hereby declare that all information in this document has been obtained and presented in accordance with academic rules and ethical conduct. I also declare that, as required by these rules and conduct, I have fully cited and referenced all material and results that are not original to this work.

Name, Last Name: HÜSEYİN YILDIZ

Signature :

ABSTRACT

PARAMETER ESTIMATION OF MULTICOMPONENT MICRO-DOPPLER SIGNALS

YILDIZ, HÜSEYİN

M.S., Department of Electrical and Electronics Engineering

Supervisor : Prof. Dr. Mete Severcan

June 2014, 80 pages

Vibrating and rotating parts on a radar target is known to generate frequency modulated echo signal which is called micro-Doppler signal. Micro-Doppler signals are commonly modeled as the sum of sinusoidally modulated signals and the parameters, such as amplitude, frequency, phase, of these modulations are useful in the identification of these targets. In this thesis, the parameters of micro-Doppler signals from helicopter targets are estimated for the classification of the helicopters. Time-frequency analysis and Hough transform is used for the separate extraction of the number of blades, blade length and angular velocity of the rotor. The algorithm is developed for a pulse-Doppler tracking radar. The performance of the proposed algorithm is tested for different SNR values. The effectiveness of different time-frequency distribution methods on the parameter extraction technique is analyzed.

Keywords: micro-Doppler, time-frequency distribution, Hough transform, helicopter blade signal, parameter estimation

ÖZ

ÇOK BİLEŞENLİ MİCRO-DOPPLER SİNYALLERİNİN PARAMETRE KESTİRİMİ

YILDIZ, HÜSEYİN
Yüksek Lisans, Elektrik ve Elektronik Mühendisliği Bölümü
Tez Yöneticisi : Prof. Dr. Mete Severcan

Haziran 2014 , 80 sayfa

Hedef platformlar üzerinde bulunan titreşen ve dönen parçaların, radar sinyalleri üzerinde mikro-Doppler adı verilen frekans modülasyonlu yankı sinyallerine sebep olduğu bilinmektedir. Mikro-Doppler sinyalleri, çoğunlukla sinüzoidal modülasyonlu sinyallerin toplamı olarak modellenmektedir. Bu tip modülasyonların genlik, frekans ve faz gibi parametreleri, hedeflerin tanımlanmasında kullanılabilecek parametlerdir. Bu tezde, helikopterlerin tanımlanması amacı ile, helikopterlerden yansıyan mikro-Doppler sinyallerinin parametreleri kestirilmektedir. Helicopterlerin pervane uzunluklarının, pervane sayılarının ve pervanelerin açısal hızlarının ayrı ayrı hesaplanması için zaman-frekans analizi ve Hough dönüşümü yöntemleri kullanılmaktadır. Bu çalışmadaki algoritma darbe-Doppler izleme radarları için geliştirilmiştir. Algoritmanın performası farklı sinyal-gürültü oranları için test edilmiştir. Farklı zaman-frekans dağılımı tekniklerinin parametre çıkarım algoritmasının başarımı üzerindeki etkisi analiz edilmiştir.

Anahtar Kelimeler: mikro-Doppler, zaman-frekans dağılımı, Hough dönüşümü, helikopter pervane sinyali, parametre kestirimi

To my fiancée

ACKNOWLEDGMENTS

Firstly, I would like to express my sincere thanks to my supervisor Prof. Dr. Mete Severcan for his supervision and guidance throughout this study.

I am indebted to my family for their continuous love, encouragement, and support during my academic studies.

I would like to thank my fiancée Elif Seyhan for her understanding and encouragement throughout my thesis study.

TABLE OF CONTENTS

LIST OF TABLES

TABLES

LIST OF FIGURES

FIGURES

LIST OF ABBREVIATIONS

c	speed of light [m/s]
L	blade length [m]
n	number of main rotor blades
RCS	radar cross section
rps	revolutions per second
STFT	short time Fourier transform
WVD	Wigner-Ville distribution
PWVD	pseudo Wigner-Ville distribution
SPWVD	smoothed pseudo Wigner-Ville distribution
pri	pulse repetition interval
prf	pulse repetition frequency
CWD	Choi-Williams distribution
GDLD	Guo-Duran-Lee distribution
m-D	micro-Doppler
CP	cubic phase
IF	intermediate frequency
IFR	instantaneous frequency rate
COHO	coherent oscillator
PLL	phase locked loop
MTI	moving target indicator
snr	signal to noise ratio
PSNR	peak signal to noise ratio
CFAR	constant false alarm ratio
CA-CFAR	cell averaging constant false alarm ratio
CUT	cell under test
pfa	probability of false alarm
RMSE	root mean squre error
LFM	linear frequency modulation

CHAPTER 1

INTRODUCTION

Classification of the detected airborne targets in a combat situation has become increasingly important with the advances in airborne strike power. Helicopters are special air targets for example which has the capability to hide in a terrain or forested area, then suddenly appear. Because of this reason, it is highly desired to identify the detected helicopter for a radar system.

To classify and identify a target, distinguishing features of the target should be extracted. For this purpose, several methods are proposed. Each of them are using different features of the radar system and the target. In this work, we concentrate on the micro-Doppler features of the returned signal. If a structure on the observed target has rotation or vibration relative to its main body translation, it causes a frequency modulation on the returned radar signal. This frequency modulations generates additional spectral sidebands around the target's bulk Doppler frequency shift, which is defined as the micro-Doppler effect [7] [5] [8]. The sources of vibrations or rotations that cause micro-Doppler effect may be propellers of a fixed-wing aircraft, rotors of a helicopter, or the engine compressor, blade assemblies of a jet aircraft, swinging limbs of a human being, an engine-induced vibrating surface of a truck and so on. Returned radar signals from these structures contain micro-Doppler characteristics related to them. Therefore, micro-Doppler signatures of the target dynamic parts can be used for target detection, recognition and classification.

Main rotor blade dynamics of a helicopter can be extracted by using micro-Doppler signatures of returned radar signal. A helicopter can be identified by its blade parameters which are blade length and number of blades [25]. The angular velocity of the

rotor may be an important blade parameter, but it may change while flying.

A helicopter consists of three main scattering centers. These are main body, main rotor and tail rotor. The RCS of the main rotor is significantly larger than the other two. If we compare the main and tail rotors, main rotor blades have larger RCS than the tail rotor blades. Also, the rotation rate of tail rotor blades are higher and the length of its blades are shorter than the main rotor blades [9]. Because of these reasons, processing the micro-Doppler signatures of the main rotor blades is a more suitable choice for target classification.

To analyze time-varying micro-Doppler signature, traditional techniques such as Fourier transform are unable to provide time-dependent frequency information. Therefore, joint time-frequency analysis is needed. However, low resolution time-frequency analysis techniques such as short time Fourier transform, do not provide the required resolution to extract micro-Doppler signatures [24]. Therefore, high resolution linear and quadratic time-frequency (TF) analysis techniques are recently employed for extracting m-D features.

1.1 Related Works

Several methods are analyzed to deal with micro-Doppler signatures and to extract blade parameters from the helicopter return signal. The wavelet analysis of helicopter data, along with the TF representation based imaging system, is presented in [9]. However, in that work, blade length and number of blades were not determined unambiguously. One of the parameters, blade length, number of blades or rotation rate of the rotor is assumed to be known. A different method for analyzing micro-Doppler signatures is proposed in [38]. In this work, the authors obtain time-frequency rate distribution instead of time-frequency distribution by using cubic phase function. After getting time-frequency rate distribution, they apply generalized Hough transform to extract the micro-Doppler features. However, the cubic phase function is defined for the polynomial phased signals with maximum degree of 3 while the phase modulation of blade echo is sinusoidal. In [40], the blade parameters are estimated based on Maximum Likelihood methods and the corresponding Cramér-Rao bounds are de-

rived. In [4], blade parameters are extracted based on inverse radon transform. In [41], it is proposed that helicopters can be classified by the ratio L/N of the blade length and number of blades. These parameters can be extracted by using Doppler spectrum and time signal. However, the L/N technique has drawbacks, since significant number of helicopters have the same quotient. In [42] time-frequency analysis of the Doppler spectrum is suggested to determine the number of blades by counting the sinusoidal traces created by blade tip in the time-frequency distribution.

1.2 Our Approach

In this study, a technique based on time-frequency analysis and Hough transform is investigated to extract helicopter blade parameters from micro-Doppler signatures of the blade return signal for the purpose of target recognition. To get the time frequency distribution, Cohen's class of distributions are used to reach the necessary resolution. After getting the time-frequency distribution image, flash period of the approaching blades are extracted. Then, maximum tip Doppler frequency of returned signal is estimated using the spectrum of flashes. Finally, using extracted parameters, Hough transform is applied to the time-frequency image to find the blade parameters.

1.3 Outline

First of all, the mathematical model for helicopter blade return signal is derived in Chapter 2, for different number of blades, blade lengths and angular velocities. Then, in Chapter 3, time-frequency distribution techniques which are short time Fourier transform, Wigner-Ville, pseudo-Wigner-Ville, smoothed pseudo-Wigner-Ville, Choi-Williams and Guo-Durand-Lee distributions are analyzed. Cohen's time frequency class is explained. The cubic phase function is also described in that chapter. In Chapter 4, the algorithm used in this work is described and analyzed. The results of the proposed algorithm is given in Chapter 5. The results are given for different helicopters, different SNR values and different time-frequency techniques(SPWVD, CWD, GDLD). Finally, Chapter 6 concludes with the evaluation of obtained results and a discussion of future work.

CHAPTER 2

OVERVIEW OF RADAR DOPPLER EFFECT AND MODELING HELICOPTER BLADE RETURN SIGNAL

In this chapter, Doppler effect and helicopter return signal will be analyzed. First, radar return signal from a point scatterer will be derived. After that, the Doppler effect in the return signal will be presented. Then, the concept of micro-Doppler will be described and the helicopter blade return signal will be derived.

2.1 Review Of Doppler Effect

Transmitted radar signal in the complex form can be written as

$$x(t) = a(t)\exp[j2\pi F_t \times t + \theta(t)] \tag{2.1}$$

where $a(t)$ is the constant amplitude pulse envelope, F_t is the transmitted carrier frequency and $\theta(t)$ is phase term or the phase modulation term.

The return signal from a point target is a delayed version of the transmitted pulse. This time delay is related to the range of the scatterer and can be calculated from the two-way trip time as

$$\Delta t = 2 \times R(t)/c. \tag{2.2}$$

The amplitude of the return signal is also different from the transmitted signal because

of the propagation loss and the radar cross section (RCS) of the target. Thus, the return signal model from a point scatterer at range $R_0 = c\Delta t/2$ is

$$s(t) = b(t - \Delta t)\exp[j2\pi F_t \times (t - \Delta t) + \theta(t - \Delta t)] + n(t) \tag{2.3}$$

where $b(t)$ is return signal pulse envelope, $\theta(t)$ is echo signal phase term and $n(t)$ is additive receiver noise [2].

If we assume that there is no phase modulation on the pulse, $\theta(t)$ becomes constant, θ, and the return signal in Equation 2.3 can be rewritten as

$$s(t) = b(t - \Delta t)\exp[j2\pi F_t \times (t - \Delta t) + \theta] + n(t). \tag{2.4}$$

The phase of the return signal (ignoring the noise) is

$$\phi(t) = 2\pi F_t \times (t - \Delta t) + \theta. \tag{2.5}$$

The instantaneous frequency of the return signal can be calculated as

$$\begin{aligned} F_r(t) &= \frac{1}{2\pi} \times \frac{d\phi(t)}{dt} \\ &= F_t \times (1 - \frac{d\Delta t}{dt}). \end{aligned} \tag{2.6}$$

If we analyze Equation 2.6, the only time dependent term is Δt. As given in Equation 2.2, if the range between the target and the radar is constant, Δt is not time dependent and $\frac{d\Delta t}{dt} = 0$. Because of this reason, instantaneous received frequency F_r becomes constant and equals to the transmitted carrier frequency F_t of the radar.

2.1.1 Doppler Effect

When electromagnetic signal interacts with a scatterer which has a motion, some properties of the signal change. From these changes, one can deduce the motion

of the scatterer with respect to the transmitter. When radar waves interacts with a moving target, the carrier frequency of the returned signal will be shifted [7]. If the range between target and the radar is not constant, the instantaneous frequency of received signal F_r will differ from the transmitted carrier frequency F_t, because of the *Doppler effect*. The theory of special relativity can explain the Doppler effect. Suppose the target is moving with a constant range rate $v(t)$ toward the radar, special relativity theory can predict the received frequency, as given in [1], as

$$F_r = \frac{1 + v/c}{1 - v/c} \times F_t. \tag{2.7}$$

If the range rate is constant in Equation 2.7, $F_r(t)$ becomes F_r. Equation 2.7 can be rewritten in a binomial series as

$$\begin{aligned} F_r &= (1 + \frac{v}{c}) \times [1 + \frac{v}{c} + (\frac{v}{c})^2 + ...] \times F_t \\ &= [1 + 2\frac{v}{c} + 2(\frac{v}{c})^2 + \ldots] \times F_t. \end{aligned} \tag{2.8}$$

For a real target, it is very obvious that the speed of light is much higher than the speed of the target ($\frac{v}{c} \ll 1$). In Equation 2.8, we can ignore all second order and higher terms without loosing significant information [2]. Then, the received signal frequency is

$$F_r = [1 + \frac{2v}{c}] \times F_t. \tag{2.9}$$

The *Doppler frequency*, defined as the difference between received and the transmitted frequency, can be obtained as [2]

$$\begin{aligned} F_D &= F_r - F_t \\ &= [1 + \frac{2v}{c}] \times F_t - F_t \\ &= \frac{2v}{c} \times F_t \\ &= \frac{2v}{\lambda_t} \end{aligned} \tag{2.10}$$

where λ is the transmitted wavelength.

2.1.2 Stop And Hop Assumption

Basically in this approximation, it is assumed that the target remains stationary during the flight of the radar pulse. At time $t = t_0$ target is stationary at range R_0 and assumed staying unmoving during the trip time of the pulse. Then, the target *hops* to position $R(t) = R_0 - v \times T$ and *stops* there, when the next pulse is transmitted and so forth. Hence, the situation is modeled as if the target is stationary at the range R_m when the m_{th} pulse is transmitted.

If the target has constant range rate, $R(t)$ becomes = $R_0 - v \times t$ and Equation 2.2 can be modified as

$$\Delta t = 2 \times \frac{R_0 - v \times t}{c}. \tag{2.11}$$

Note that in Equation 2.11, we assume that the target is stationary while the pulse is traveling (stop-and-hop assumption).

Then, the received signal phase in Equation 2.5 becomes

$$\phi(t) = 2\pi F_t \times (t - 2 \times \frac{R_0 - v \times t}{c}) + \theta. \tag{2.12}$$

The Doppler frequency is the difference between the received and the transmitted signal frequencies [2]. As described above, frequency of the signal can be calculated by taking the derivative of the phase of the signal with respect to time. If we change the phase in Equation 2.6, received signal frequency is calculated as

$$\begin{aligned} F_r &= \frac{1}{2\pi} \times \frac{\delta\phi(t)}{\delta t} \\ &= F_t \times (1 - \frac{\delta\Delta t}{\delta t}) \\ &= F_t \times (1 + \frac{2v}{c}) \end{aligned} \tag{2.13}$$

The corresponding Doppler frequency can be calculated as

$$\begin{aligned} F_D &= F_r - F_t \\ &= F_t \times (1 + \frac{2v}{c}) - F_t \\ &= \frac{2vF_t}{c} \\ &= \frac{2v}{\lambda_t}. \end{aligned} \tag{2.14}$$

Note that the calculated Doppler above is same as the calculated Doppler in Equation 2.10. This result shows us that the stop and hop assumption gives reliable accuracy.

2.2 Micro-Doppler Effect

In the previous section, we have seen that the Doppler frequency shift created by the target which has constant radial velocity with respect to radar is time-invariant. However, the Doppler frequency shift generated by micro-motion dynamics of the target can be a time-varying function. This motion imposes a time-varying modulation onto the frequency as described in [9]. This modulation is called *micro-Doppler effect*.

The micro-Doppler effect can be caused by rotating structures, such as propellers of a fixed-wing aircraft, rotors of a helicopter, or vibrating structures [7]. This feature enables us to know the dynamic properties of the targets such as knowledge about the blade numbers and blade speed of the helicopter.

To analyze micro-Doppler signature of a vibrating target, consider the geometry shown in Figure 2.1. The point target located at point P is vibrating between points G to G' ,distance D_v, with oscillation frequency of f_v. Then, the time delay in Equation 2.2 turns into

$$\Delta t = 2 \times [R_0 - v \times t + D_v \cos(\beta) \sin(2\pi f_v t + \phi_0)]/c \tag{2.15}$$

where R_0 is the initial range, v is the target body's range rate, β is the angle between vibration direction and the radar-target line and ϕ_0 is the initial phase of the vibration.

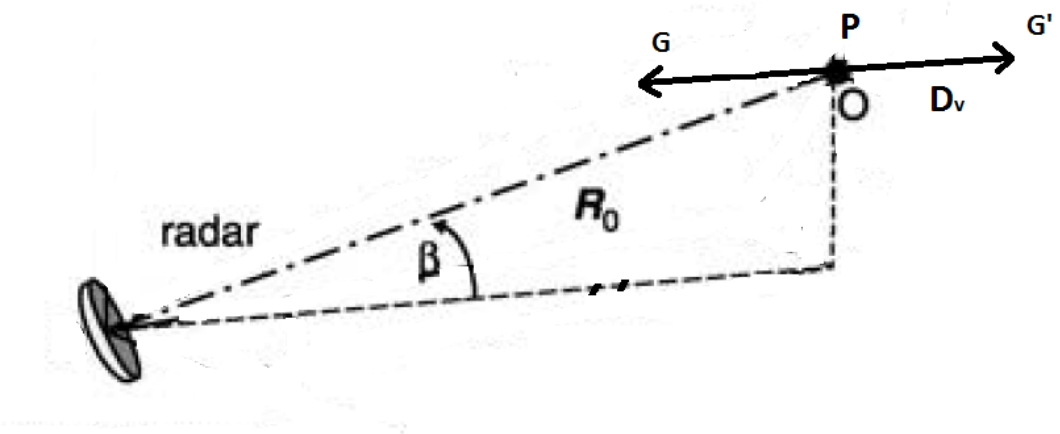

Figure 2.1: Geometry of a vibrating target.

Assume that the initial phase of the vibration ϕ_0 and the initial phase of the signal θ are 0. Then, using the time delay in Equation 2.15, the received baseband signal becomes

$$s(t) = \sigma \exp[-j\frac{4\pi}{\lambda} \times (R_0 - v \times t + D_v \cos(\beta) \sin(2\pi f_v t))] \tag{2.16}$$

and the baseband phase in Equation 2.12 becomes

$$\phi(t) = -\frac{4\pi}{\lambda} \times (R_0 - v \times t + D_v \cos(\beta) \sin(2\pi f_v t))). \tag{2.17}$$

Therefore, the Doppler frequency is obtained as

$$\begin{aligned} F_D(t) &= \frac{1}{2\pi} \times \frac{d\phi(t)}{dt} \\ &= -\frac{2}{\lambda} \times (-v + 2\pi D_v f_v \times \cos(\beta) \cos(2\pi f_v t)) \\ &= \frac{2v}{\lambda} - \frac{4\pi D_v f_v \times \cos(\beta) \cos(2\pi f_v t)}{\lambda}. \end{aligned} \tag{2.18}$$

As shown in Equation 2.18, the Doppler frequency is not constant but time dependent because of the micro motions of the target. The first term $\frac{2v}{\lambda}$ is the Doppler frequency caused by the main target motion while the second term $-\frac{4\pi D_v f_v \times \cos(\beta)\cos(2\pi f_v t)}{\lambda}$ is the micro-Doppler modulation term.

Assume a radar with wavelength $\lambda = 0.03$ m tracking a target which is stationary but vibrant. The amplitude of the vibration D_v is 0.01 meters and the vibration frequency f_v is 2 Hz. The elevation angle β is $60°$. With this configuration, the result of Equation 2.18 can be seen in Figure 2.2.

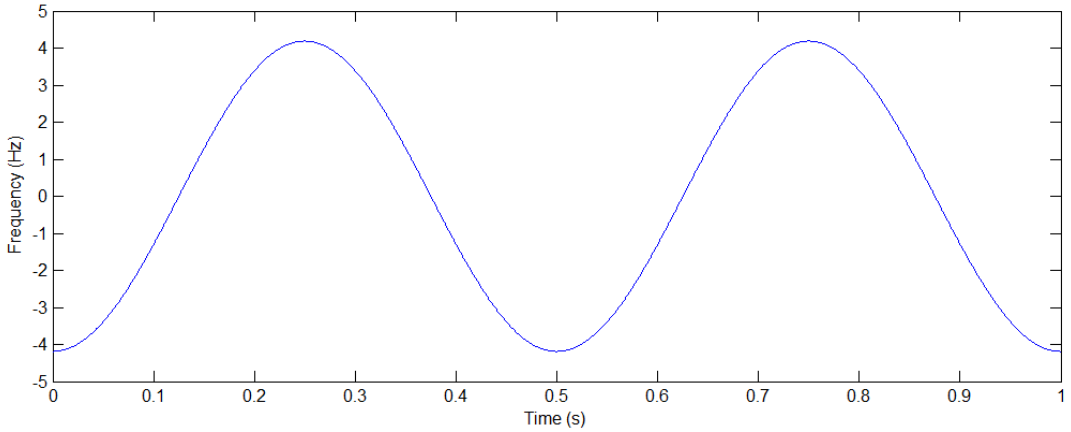

Figure 2.2: Time-frequency micro-Doppler signature calculated by Equation 2.18.

The micro-Doppler modulation generates sidebands about the targets main motion's Doppler frequency shift. Because of this reason, in order to demodulate these micro-Doppler frequencies, coherent processing must be used to track the phase change of the target [7].

Traditional analysis like Fourier transform or the short time Fourier transform can not be sufficient to supply necessary resolution to demodulate these signal components. Because of this reason, higher-resolution time–frequency analysis tools are required [8].

2.3 Modeling Blade Return Signal

In this section, we derive an analytical model for the main rotor blade echoes described in both [5] and [3]. Each blade is taken as a straight wire segment. Before

starting derivation, it is very helpful to assume that:

- there is no blind region
- the target is tracked in Doppler domain, so the Doppler effect of the body of the helicopter is compensated and the return signal is modeled only with the blade Doppler frequency.
- all points of the blade is in the main lobe of the antenna.
- range between the target and the radar is much larger than the blade length.
- returned signal amplitude is the reflectivity coefficient of the scatterer.

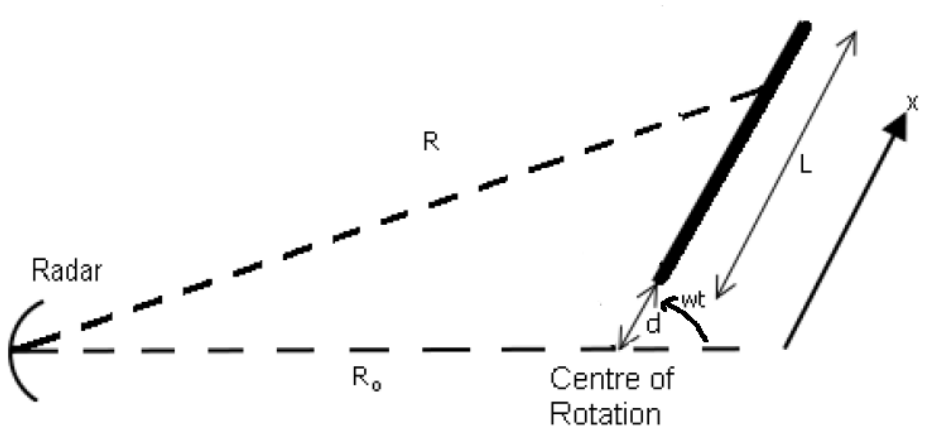

Figure 2.3: Geometry of a rotating wire [4].

Our blade is modeled as continuous point targets along a wire in one dimension [3]. As seen in Figure 2.3, the straight wire of length L is radially oriented at center of rotation point . The length d is the blank region between rotation center and the blade root.

Let x be a scattering point on the wire, then the range R of the point scatterer x to the radar at time t is

$$R(t) = \sqrt{R_{body}^2 + x^2 + 2 \times R_{body} x \cos(wt)} \tag{2.19}$$

where w is the angular velocity of the blades and the $R_{body}(t)$ is the range of the body of the helicopter. The Equation 2.19 stands for the *law of cosines*. Assuming $R_0 \gg x$ so $(x/R_{body}(t))^2 \mapsto 0$ in the far field [5], Equation 2.19 becomes

$$R(t) = R_{body}(t) + x\cos(wt). \tag{2.20}$$

If there is an elevation angle β between the radar and the target helicopter (assuming target helicopter is parallel to the ground, as described in [5]), Equation 2.20 becomes

$$R(t) = R_{body}(t) + x\cos(wt)\cos(\beta) \tag{2.21}$$

and the time delay for the signal is

$$\begin{aligned} \Delta t &= 2 \times \frac{R(t)}{c} \\ &= 2 \times \frac{R_{body}(t) + x\cos(wt)\cos(\beta)}{c}. \end{aligned} \tag{2.22}$$

For the range function in 2.21 the return signal in Equation 2.4 becomes

$$\begin{aligned} s(t) &= b(t-\Delta t)\exp[j2\pi F_t \times (t-\Delta t)] \\ &= \sigma\exp[j2\pi F_t \times (t - 2 \times \frac{R_{body}(t) + x\cos(wt)\cos(\beta)}{c})] \\ &= \sigma\exp[j2\pi F_t \times t - 4\pi \times \frac{R_{body}(t)}{\lambda} - 4\pi \times \frac{x\cos(wt)\cos(\beta)}{\lambda}] \\ &= \sigma\exp[j2\pi F_t \times t - \frac{4\pi\cos(\beta)}{\lambda} \times x\cos(wt) - \phi] \end{aligned} \tag{2.23}$$

where sigma is the reflectivity of the point scatterer x and ϕ is the phase term with respect to the range of the body of the helicopter. At the beginning of this section, we assumed that the radar is a Doppler tracking radar and the target's body Doppler frequency is shifted to zero by the radar receiver. Therefore, the returned baseband signal is

$$s(t) = \sigma\exp[-j\frac{4\pi\cos(\beta)}{\lambda} \times x\cos(wt)] \tag{2.24}$$

Equation 2.24 gives the return signal for one scatterer, for a wire shown in Figure 2.3, ignoring the scatterer free region d, the total signal is

$$s(t) = \int_0^L \sigma \exp[-j\frac{4\pi\cos(\beta)}{\lambda} \times x\cos(wt)]dx \tag{2.25}$$

This integration leads to an exact analytical result [5], which is

$$s(t) = \sigma L \times \exp[-j\frac{4\pi\cos(\beta)}{\lambda}\frac{L}{2} \times \cos(wt)] \times \text{sinc}[\frac{4\pi\cos(\beta)}{\lambda}\frac{L}{2} \times \cos(wt)] \tag{2.26}$$

where sinc(x) $= \sin(x)/x$, $x \neq 0$ and sinc(0) $= 1$. As explained in [3], this $sinc$ term describes the amplitude modulation of the signal in time and the periodic $\cos(wt)$ function inside the sinc function that describes the characteristic blade flashes of the helicopter return signal.

Suppose a helicopter has one blade. The length of the blade is 6 meters and the rotation speed of 300 rpm. This helicopter is tracked with a pulsed Doppler radar with the carrier frequency of 10 GHz and pulse repetition frequency of 40 kHz. Assume there is no reflection from the body and the tail blades of the helicopter and there is no noise and vibration. The return signal calculated from the mathematical derivations can be seen in Figure 2.4.

Figure 2.4a shows the time domain signal. As seen in Figure 2.4a, there are flashes when blades are perpendicular to the radar line of sight at which the RCS of the blade is maximum, as described in [3]. The flash period is 0.1 seconds while the rotation speed is 300 rpm (which means that the period of rotation is 0.2 seconds). The flashes occur two times in one period, first one occurs while approaching, the second occurs while receding.

Figure 2.4b shows the Fourier transform of the received signal. The power is uniformly distributed over a large band. This distribution is symmetric about the 0 frequency. The limits are determined by the maximum Doppler frequency of the

helicopter blades. Maximum received Doppler frequency can be calculated as

$$\begin{aligned} f_{max} &= \frac{2 \times v_{max}}{\lambda} \\ &= \frac{2 \times wL}{\lambda} \\ &= \frac{4 \times pi \times 5 \times 6}{0.03} \\ &= 12566\, Hz \end{aligned} \tag{2.27}$$

the power is distributed along the $-f_{max}\ -\ +f_{max}$.

Figure 2.4c is the spectrogram of the return signal which gives more information than the first two, because one can see both time and frequency properties of the signal on the same graph. The figure shows the evolution of spectrum as blade rotates. Again the flashes can be seen from the figure. The first flash at time 0.05 is the flash corresponding to the approaching blade, the second is due to the receding blade, because the first has positive frequencies, while the second has negative frequencies.

Equation 2.26 gives us the baseband return signal for one blade of a helicopter. The total returns from the blades can be calculated by summing the returns from every blade. Blades are uniformly separated in angle, so that the phase difference of k^{th} blade is

$$\phi_k = \frac{2\pi k}{N} \tag{2.28}$$

where N is number of blades. Then, the total return signal can be calculated as

$$\begin{aligned} s(t) = \sum_{k=0}^{N-1} \sigma L \times \exp[-j\frac{4\pi\cos(\beta)}{\lambda}\frac{L}{2} \times \cos(wt + \frac{2\pi k}{N})] \\ \times \text{sinc}[\frac{4\pi\cos(\beta)}{\lambda}\frac{L}{2} \times \cos(wt + \frac{2\pi k}{N})] \end{aligned} \tag{2.29}$$

where the initial phase of the first blade is 0. If the phase of first blade is not equal to 0, in Equation 2.29, $\cos(wt + \frac{2\pi k}{N})$ terms should be replaced by $\cos(wt + \frac{2\pi k}{N} + \theta_0)$.

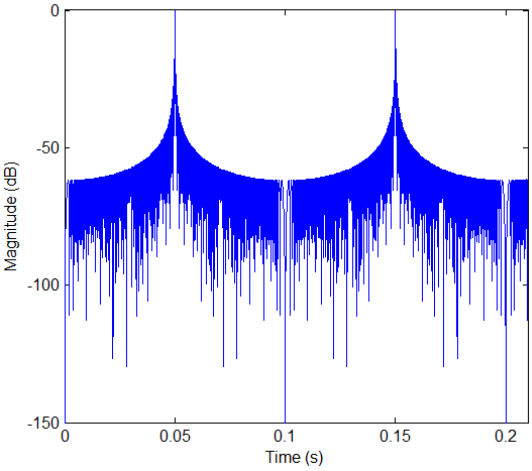

(a) Time domain return signal

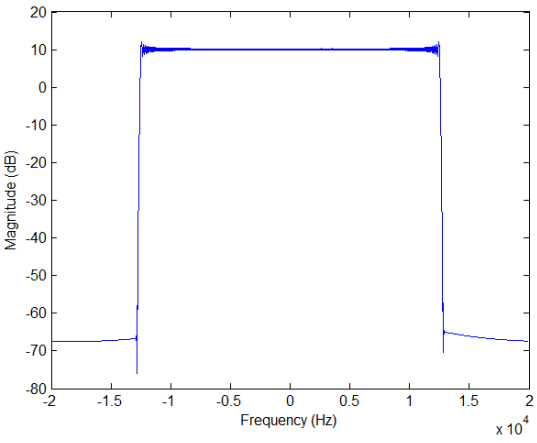

(b) FFT of return signal

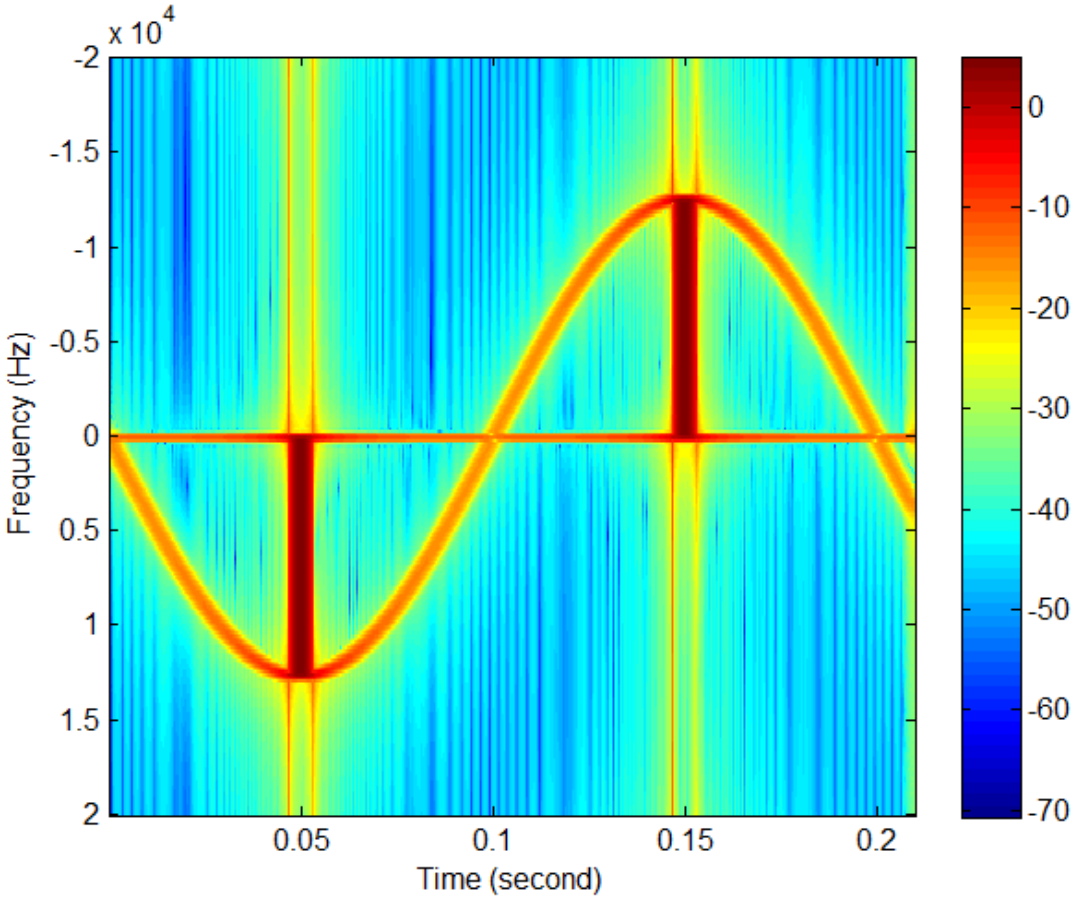

(c) Spectrogram of return signal

Figure 2.4: Time and frequency plots of one blade return signal. Plots are normalized to peak signal.

Figure 2.5 shows the return signal in time and frequency domains for four blades. In Figure 2.5c, the flashes occurs more often compared to single blade. Another difference is while n^{th} blade is receding, the $(n+2)^{th}$ blade is approaching. Because of this reason, at the flash time, there are both positive and negative frequencies.

Figure 2.6 shows the return signal in time and frequency domains for five blades. The difference between five blades and four blades is, while one blade flashes, no other blade is perpendicular to the radar.

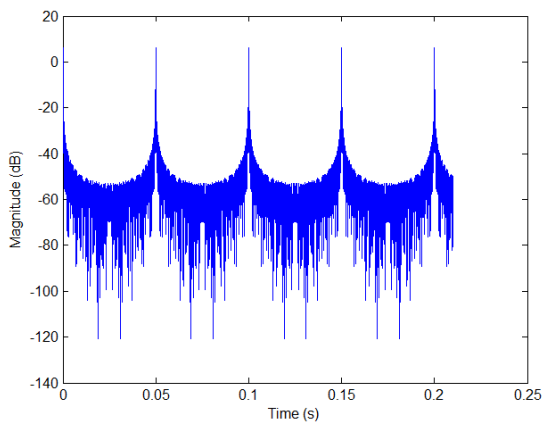

(a) Time domain return signal

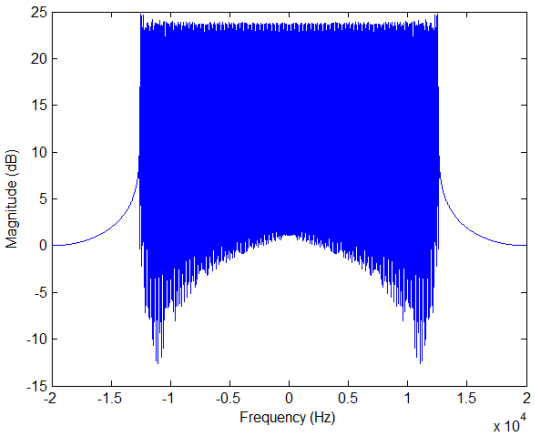

(b) FFT of return signal

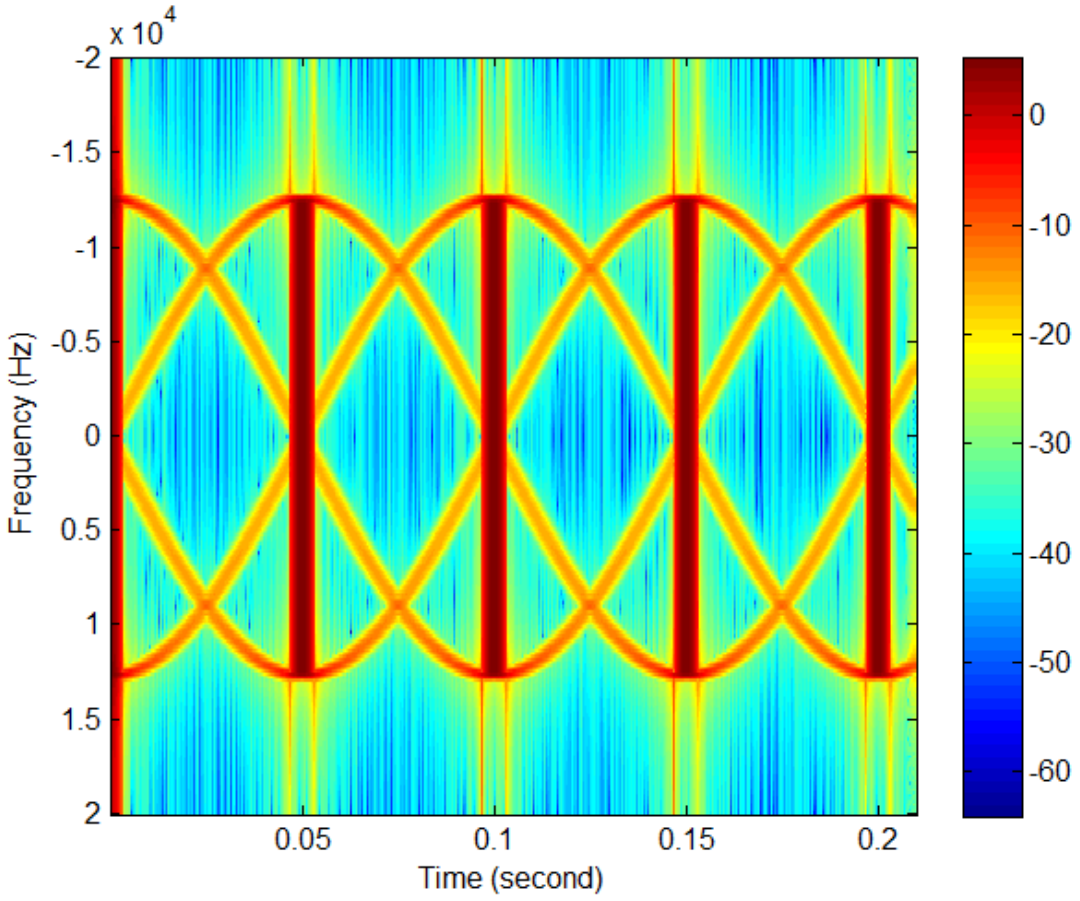

(c) Spectrogram of return signal

Figure 2.5: Time and frequency plots of four blade return signal. Plots are normalized to peak signal.

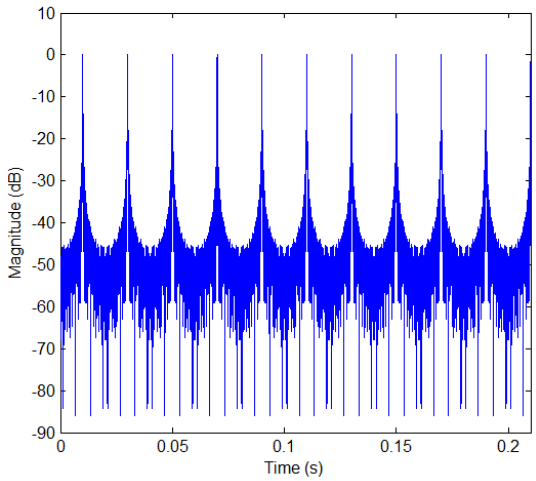

(a) Time domain return signal

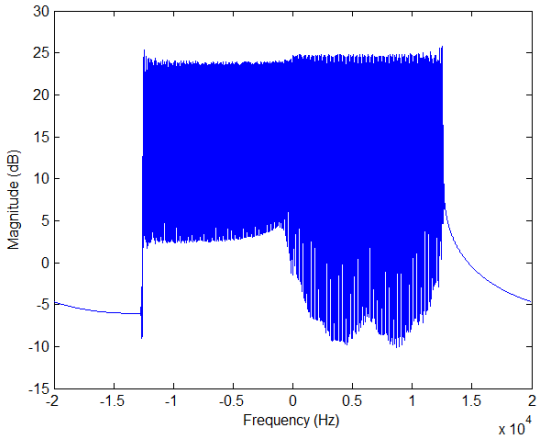

(b) FFT of return signal

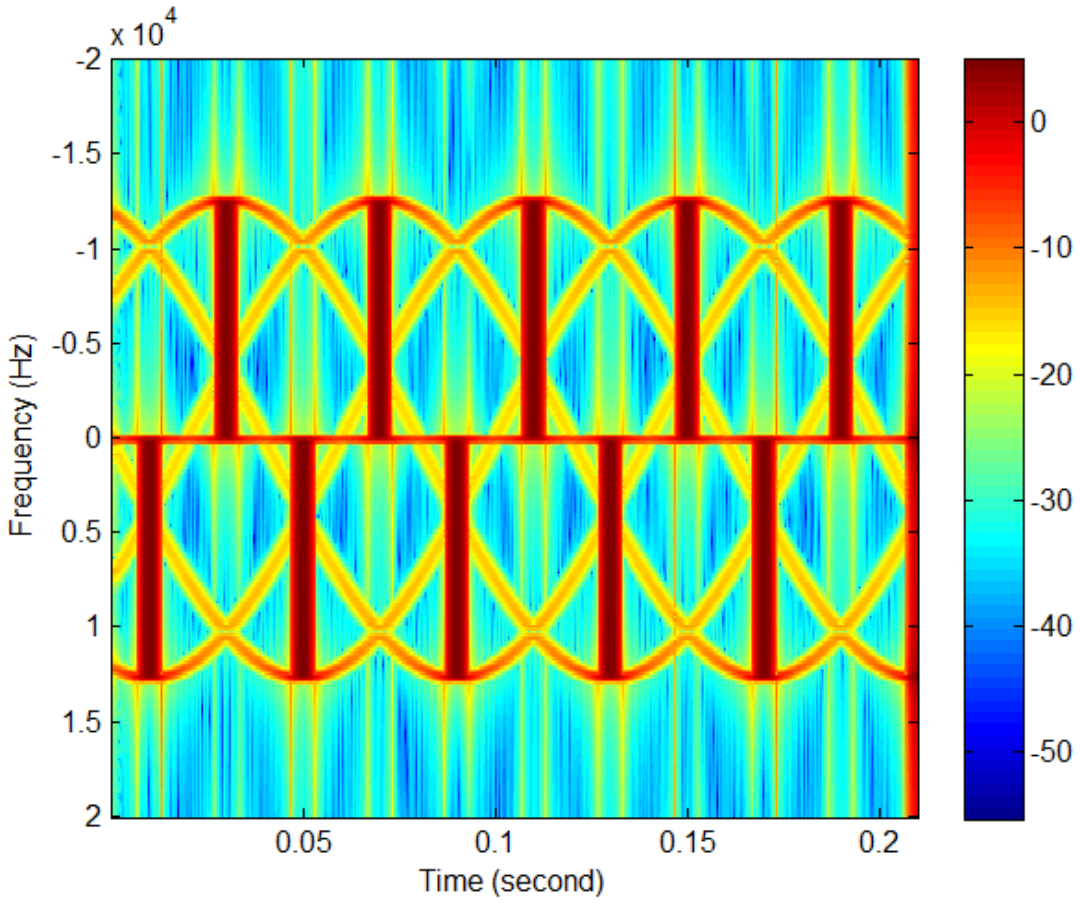

(c) Spectrogram of return signal

Figure 2.6: Time and frequency plots of five blade return signal. Plots are normalized to peak signal.

CHAPTER 3

OVERVIEW OF TIME FREQUENCY TRANSFORMS

In this chapter, the joint time-frequency analysis techniques will be discussed in detail. First, the shortcomings of the standard Fourier transform will be discussed. After that the short time Fourier transform will be explained following which the bilinear transforms Wigner-Ville, Choi-Williams and Guo-Durant-Lee distributions, will be considered. Cubic phase function, which is a time-frequency rate distribution, will also be analyzed in this chapter.

3.1 Introduction

Standard Fourier Transform gives information about frequency characteristics of the signal. The basic idea of Fourier transform is expressing the signal in terms of sinusoids with different frequencies and amplitudes. The output of Fourier transform is amplitudes of each frequency components inside the signal. However, if the frequency of the signal changes with time, spectrum can not give the information about the relationship between frequency change and time. Fourier transform can not provide simultaneous time and frequency localization. It is not useful for non-stationary signals. For example, for LFM (linear frequency modulation) signals, the frequency of the signal changes continuously as time goes by. The spectrum of the LFM signal gives only the bandwidth information about the modulation. The difference between spectrum and joint time-frequency analysis is, while spectrum gives the existing frequencies, the joint time-frequency analysis gives which frequencies existed at a particular time [10].

The basic idea in joint time-frequency transformation is to find a joint function of both time and frequency that will describe the energy density of a signal simultaneously both in time and frequency. This function must conserve the energy of the whole signal, hence

$$E = \int_{-\infty}^{+\infty} \int_{-\infty}^{+\infty} P(t,\omega) d\omega dt \tag{3.1}$$

where the $P(t,\omega)$ is the joint time-frequency function and E is the total signal energy. However, note that, there are many functions that satisfy the correct value for the total energy but that does not describe the energy density of the signal in time or frequency [10]. Because of this reason, the ***ideal*** joint density in time and frequency should satisfy the marginals which are time and frequency. Integrating the energy for all frequencies at any time should give the instantaneous energy at that time and integrating the energy over all times at any frequency should give the energy of the signal for that frequency. Consequently, as given in [6], the time marginal condition is

$$\int_{-\infty}^{+\infty} P(t,\omega) d\omega = |s(t)|^2 \tag{3.2}$$

and the frequency marginal condition is

$$\int_{-\infty}^{+\infty} P(t,\omega) dt = |S(\omega)|^2 \tag{3.3}$$

where $S(\omega)$ is the spectrum of the signal. Then, it is guaranteed that the function $P(t,\omega)$ is the ideal joint time-frequency distribution function of the signal $s(t)$. If joint density satisfies the marginals, the total energy conservation is also satisfied.

Although many distribution do not satisfy the total energy conservation, they are successful in representing the time-frequency characteristics of the signal such as *Short Time Fourier Transform*. Because of that reason, Cohen names it as "*weak one*" [6]. In addition, some of the distributions do not satisfy the marginal conditions while giving a good representation of the time-frequency like *Smoothed Wigner-Ville Distribution*.

There are many distributions developed to express the signal in time and frequency jointly. For all time frequency distributions, Leon Cohen developed a general form [10], [6], [12],

$$C(t,\omega) = \frac{1}{4\pi^2}\int\int\int s(u+\frac{1}{2}\tau)s^*(u-\frac{1}{2}\tau)\phi(\theta,\tau)e^{-j\theta t - j\tau\omega + j\theta u}dud\tau d\theta \quad (3.4)$$

In general, it can be said that there is no best time frequency distribution technique. There must be suitability between technique and the process. Therefore, Cohen's class is very important because one can design a time frequency distribution using this general form with desired parameters. The detailed explanation about Cohen's Class will be given after the definition of Wigner-Ville distribution.

3.2 Short Time Fourier Transform

The short time Fourier transform is the most widely used Fourier transform based technique for time-frequency signal analysis, because it is simple and the results are satisfactory [10]. The idea behind it is splitting the signal into overlapping sections in time and taking Fourier transform of each section of the signal, as shown below

$$S_t(\omega) = \frac{1}{\sqrt{2\pi}}\int_{-\infty}^{+\infty} e^{-j\omega t'}s(t')h(t'-t)dt' \quad (3.5)$$

where $h(t)$ is a windowing function which is normalized so as to be of unit energy [13]. Note that the only difference between the standard Fourier transform and the short time Fourier transform is the windowing function.

The sections are narrow enough to be considered as a stationary signal. The length of the window function determines the segment length. For each time location where the window is centered,we obtain a Fourier transform. Each Fourier transform provides frequency information for different time slices. Then, time dependent frequency spectrum is obtained.

The *spectrogram* is the magnitude square of the short time Fourier transform, which

is

$$P_s(t,\omega) = |S_t(\omega)|^2. \tag{3.6}$$

Figure 3.1 shows the spectrogram of the sum of two linear frequency modulated signal given below

$$s(t) = \exp[-j2\pi(-175t + 100)t] + \exp[-j2\pi(-175t + 250)t]. \tag{3.7}$$

Although this is the standard method for time frequency analysis, the signals whose frequency content is changing so rapidly are problematic for the spectrogram. Because finding an appropriate short-time window is hard. Also shortening the time window means reduction in the frequency resolution, because there is a trade off between the time and the frequency resolution. It is a well known fact that the narrower the signal in time broader its spectrum, and vice versa, and therefore accurate localization in frequency requires a wider time window while accurate localization in time requires wider frequency window. Uncertainty principle tells that it is not possible to have arbitrarily high accuracy in both time and frequency. Equation below gives this uncertainty principle

$$\sigma_t \times \sigma_\omega \geq \frac{1}{2}\sqrt{1 + 4Cov_{t\omega}^2} \tag{3.8}$$

where σ_t and σ_ω are standard deviations of time and bandwidth of the signal respectively and $Cov_{t\omega}$ is the covariance of time and instantaneous frequency of the signal. $Cov_{t\omega}$ is a measure of how time and the instantaneous frequency are related. Which is defined as

$$Cov_{t\omega} = E\{t\omega(t)\} - E\{t\}E\{\omega\} \tag{3.9}$$

In the best case, the $Cov_{t\omega}$ term becomes zero when there is no relationship between time and the instantaneous frequency. Then the $\sigma_t \times \sigma_\omega$ product becomes minimum

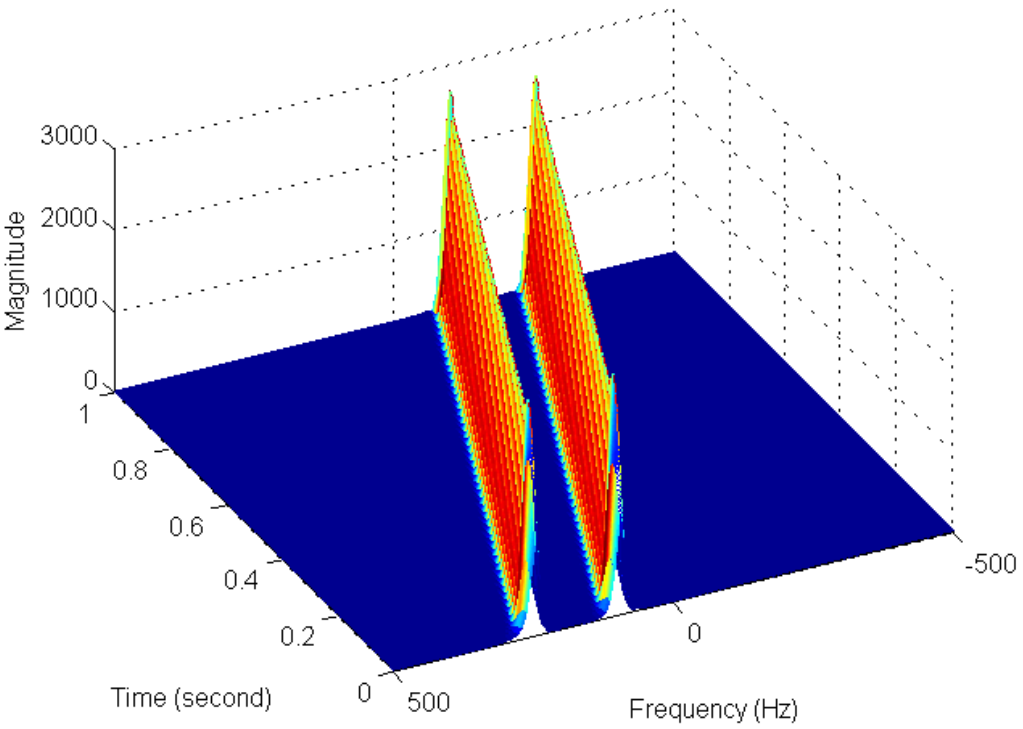

(a) 3-D mesh plot

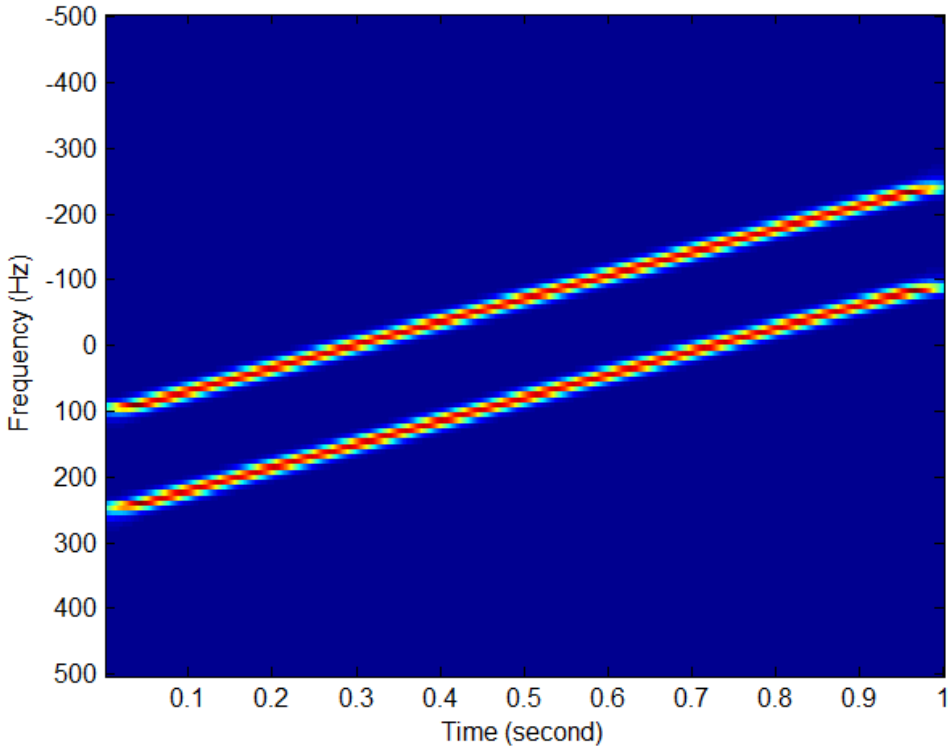

(b) 2-D plot

Figure 3.1: The Spectrogram of the sum of two chirp (Equation 3.7).

[6]. More detailed information about the uncertainty can be found in Chapter 1 and Chapter 3 of reference [6].

Spectrogram gives energy of the signal in the neighborhood of $[t-\Delta_t/2, t+\Delta_t/2] \times [\omega-\Delta_\omega/2, \omega+\Delta_\omega/2]$ area, where Δ_t and Δ_ω are the time and frequency window widths of spectrogram respectively [11]. The Δ_ω and the Δ_t can not be both selectable, only the time window width Δ_t is selectable. The other is determined by uncertainty principle given in Equation 3.8.

3.3 Wigner-Ville Distribution

The Wigner-Ville distribution is the prototype for the Cohen's class time frequency distributions that are qualitatively different from the spectrogram [6]. It was first developed by the Wigner in the area of quantum mechanics in 1932. In 1947, Ville modified it to use for signal analysis.

Wigner-Ville distribution is defined as the Fourier transform of the autocorrelation function [6]. Therefore, it can be written as

$$WVD(t,\omega) = \frac{1}{2\pi}\int R(t,\tau)e^{-j\omega\tau}d\tau \tag{3.10}$$

where the instantaneous autocorrelation function is

$$R(t,\tau) = s(t+\frac{\tau}{2})s^*(t-\frac{\tau}{2}) \tag{3.11}$$

where s^* stands for the complex conjugate of s. Substituting Equation 3.11 into Equation 3.10

$$WVD(t,\omega) = \frac{1}{2\pi}\int s(t+\frac{\tau}{2})s^*(t-\frac{\tau}{2})e^{-j\omega\tau}d\tau \tag{3.12}$$

gives the more general form of the *Wigner-Ville distribution* [14][15]. In terms of the

signal spectrum $S(\omega)$

$$WVD(t,\omega) = \frac{1}{2\pi}\int S(\omega + \frac{\theta}{2})S^*(\omega - \frac{\theta}{2})e^{-jt\theta}d\theta \tag{3.13}$$

[6]. The Wigner-Ville distribution can also be represented using ambiguity function, which is defined as the inverse Fourier transform of the autocorrelation function as shown below [16] [6]

$$A(\theta,\tau) = \int R(t,\tau)e^{j\theta t}dt. \tag{3.14}$$

Note that Equation 3.14 shows that the Ambiguity function $A(\theta,\tau)$ is the inverse Fourier transform of the autocorrelation function $R(t,\tau)$. Then $R(t,\tau)$ can be written as the Fourier transform of the ambiguity function as

$$R(t,\tau) = \frac{1}{2\pi}\int A(\theta,\tau)e^{-jt\theta}d\theta. \tag{3.15}$$

Thus, if we replace autocorrelation function with Equation 3.15, the Wigner-Ville distribution becomes

$$WVD(t,\omega) = \frac{1}{4\pi^2}\int\int A(\theta,\tau)e^{-jt\theta}e^{-j\omega\tau}d\theta d\tau. \tag{3.16}$$

Although there is no physical relationship between the Wigner-Ville distribution and the ambiguity function, this approach is very helpful to understand the Cohen's class distributions.

The main advantage of Wigner-Ville distribution over spectrogram is the higher resolution in time and frequency [16]. However, the analysis of multicomponent signals is problematic because of the cross terms between the components of the signal [17]. Suppose we express a signal as

$$s(t) = s_1(t) + s_2(t). \tag{3.17}$$

By substituting $s(t)$ into Equation 3.12, we get

$$\begin{aligned} WVD(t,\omega) &= \frac{1}{2\pi}\int s(t+\frac{\tau}{2})s^*(t-\frac{\tau}{2})e^{-j\omega\tau}d\tau \\ &= \frac{1}{2\pi}\int [s_1(t+\frac{\tau}{2})+s_2(t+\frac{\tau}{2})]\times[s_1^*(t-\frac{\tau}{2})+s_2^*(t-\frac{\tau}{2})]e^{-j\omega\tau}d\tau \\ &= \frac{1}{2\pi}\int s_1(t+\frac{\tau}{2})s_1^*(t-\frac{\tau}{2})+s_1(t+\frac{\tau}{2})s_2^*(t-\frac{\tau}{2}) \\ &+ s_2(t+\frac{\tau}{2})s_1^*(t-\frac{\tau}{2})+s_2(t+\frac{\tau}{2})s_2^*(t-\frac{\tau}{2})e^{-j\omega\tau}d\tau \\ &= WVD_{11}(t,\omega)+WVD_{22}(t,\omega)+WVD_{12}(t,\omega)+WVD_{21}(t,\omega) \end{aligned} \tag{3.18}$$

where the WVD_{11} and WVD_{22} are the Wigner-Ville distribution of the s_1 and s_2 respectively and the WVD_{12} and the WVD_{21} are the cross terms. The cross Wigner-Ville distribution is complex and $WVD_{21} = WVD_{12}^*$, therefore $WVD_{12}(t,\omega) + WVD_{21}(t,\omega)$ is real [6]. The Wigner-Ville distribution of $s(t)$, therefore, can be written as

$$WVD(t,\omega) = WVD_{11}(t,\omega)+WVD_{22}(t,\omega)+2Re\{WVD_{12}(t,\omega)\}. \tag{3.19}$$

If we analyze Equation 3.19, the Wigner-Ville distribution of the sum of two signals is not sum of two Wigner-Ville distributions. There is an extra term $2Re\{WVD_{12}(t,\omega)\}$ which is called cross term or interference term. Detailed analysis of cross terms in Wigner-Ville distribution can be found in [17], [6], [18]. Figure 3.2 shows the Wigner-Ville distribution of the signal that is sum of two chirp signal given in Equation 3.7. The cross term is exactly in between the two chirp term. This is not surprising, because any pair of signals creates one cross-term at middle of the two signals both in time and frequency [18][6][17].

3.3.1 Cohen's General Class Of Time Frequency Distributions

As described above, the cross terms are major drawback of the Wigner-Ville distribution. This phenomena may cause difficulties in interpreting the Wigner-Ville distri-

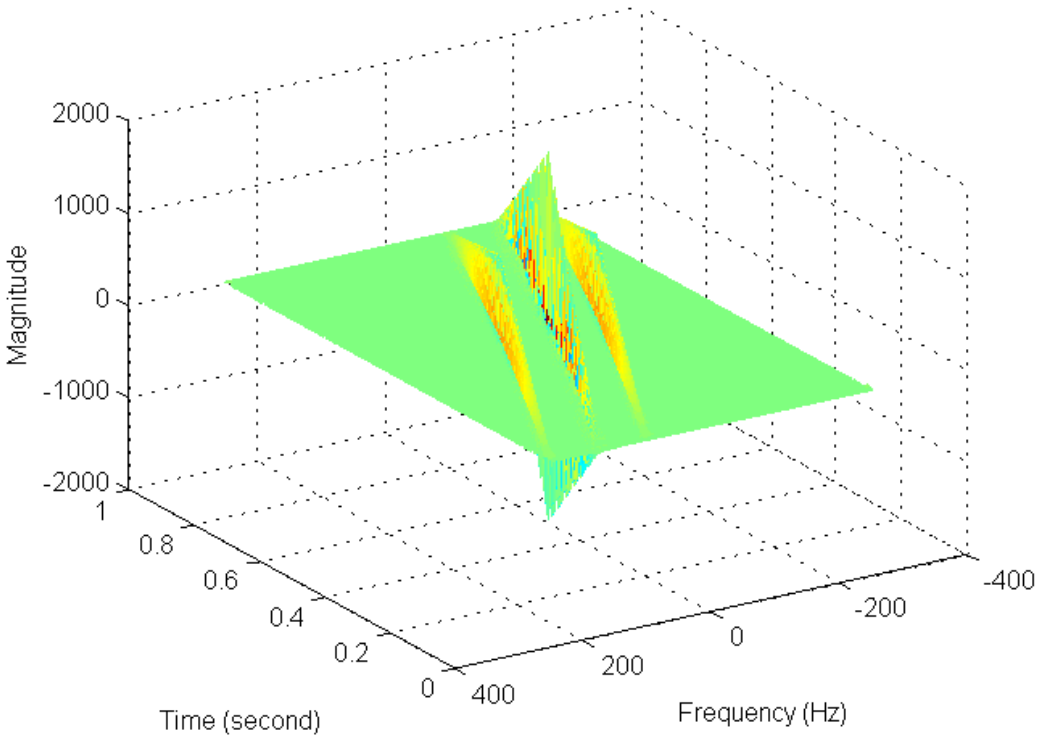

(a) 3-D mesh plot

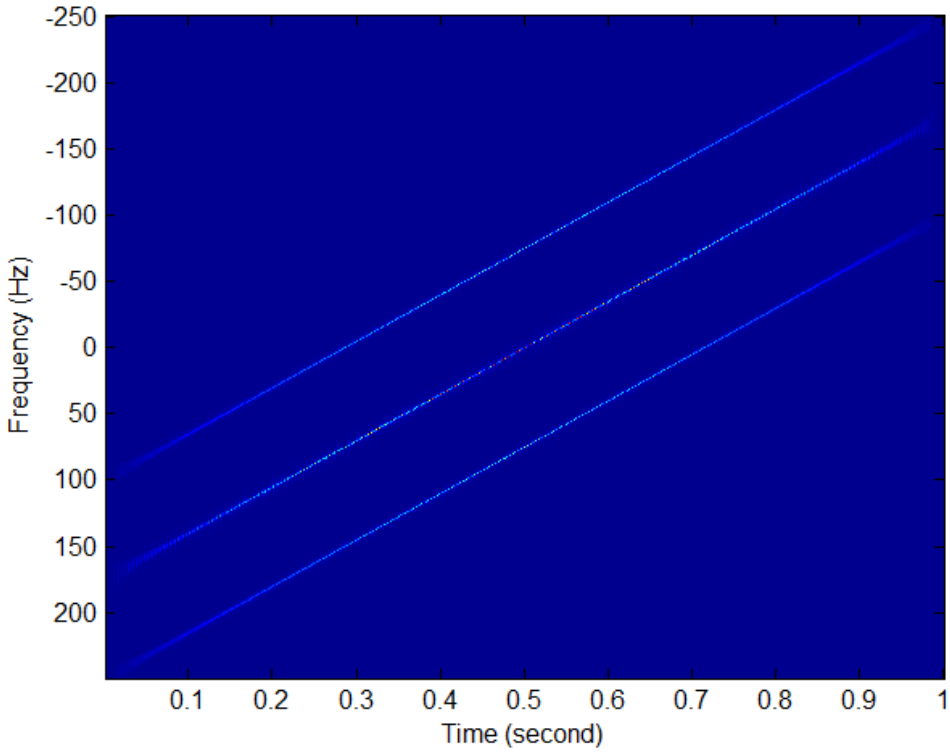

(b) 2-D plot

Figure 3.2: The WVD of the sum of two chirp with cross term (Equation 3.7).

bution as an energy distribution over time and frequency [24]. To suppress the cross terms, smoothing filters in both time and frequency can be used as

$$WVD'(t,\omega) = \int\int WVD(u,\theta)\Phi(t-u,\omega-\theta)dud\theta \tag{3.20}$$

where $\Phi(t,\omega)$ is the 2-D smoothing filter [16]. In this case, Equation 3.16 can be written as

$$WVD'(t,\omega) = \frac{1}{4\pi^2}\int\int A(\theta,\tau)\phi(\theta,\tau)e^{-j\theta t}e^{-j\tau\omega}d\tau d\theta \tag{3.21}$$

where ϕ is the kernel function for smoothing which is the 2-D inverse Fourier transform of the 2-D smoothing function $\Phi(t,\omega)$ [16]:

$$\Phi(t,\omega) = \int\int \phi(\theta,\tau)e^{-j\omega\tau}e^{-j\theta t}d\tau d\theta. \tag{3.22}$$

Note that the only difference between Equation 3.16 and Equation 3.21 is the kernel function. If we choose $\Phi(t,\omega)$ as $\delta(t)\delta(\omega)$, the $\phi(\theta,\tau)$ becomes 1 and Equation 3.20 turns into standard Wigner-Ville distribution. We can also generate the Cohen's general form for time frequency distributions from Equation 3.21, by using Equation 3.14 and Equation 3.11 as

$$\begin{aligned} WVD'(t,\omega) &= \frac{1}{4\pi^2}\int\int A(\theta,\tau)\phi(\theta,\tau)e^{-j\theta t}e^{-j\tau\omega}d\tau d\theta \\ &= \frac{1}{4\pi^2}\int\int\int R(u,\tau)\phi(\theta,\tau)e^{-j\theta t}e^{-j\tau\omega}e^{-j\theta u}d\tau d\theta du \\ &= \frac{1}{4\pi^2}\int\int\int s(u+\frac{\tau}{2})s^*(u-\frac{\tau}{2})\phi(\theta,\tau)e^{-j\theta t}e^{-j\tau\omega}e^{-j\theta u}d\tau d\theta du \\ &\triangleq C(t,\omega). \end{aligned} \tag{3.23}$$

3.3.2 Pseudo Wigner-Ville Distribution

For a given time and frequency, the standard Wigner-Ville distribution uses all times and frequencies from minus infinity to plus infinity. The summation from minus infinity to plus infinity is practically impossible. In addition, Wigner-Ville distribution weighs all times and frequencies equally. However, we may want to emphasize the properties near the time of interest. Because of these reasons, *pseudo-Wigner-Ville* distribution is introduced [19] as

$$\begin{aligned} PWVD(t,\omega) &= \frac{1}{2\pi}\int h(\tau)s^*(t-\frac{\tau}{2})s(t+\frac{\tau}{2})e^{-j\omega\tau}d\tau \\ &= \int H(\omega-\theta)WVD(t,\theta)d\theta \end{aligned} \tag{3.24}$$

where $h(t)$ is windowing function and $H(\omega)$ is Fourier transform of $h(t)$. Pseudo-Wigner-Ville distribution is the short-time Wigner-Ville distribution. It is also the smoothed version of the standard Wigner-Ville distribution. One consequence of the smoothing is the suppression of the cross terms, since we have made Wigner-Ville distribution local. While windowing, the lag suppresses the cross terms. Another result of smoothing is that it destroys many properties of the Wigner-Ville distribution such as marginal properties [20] [6]. Figure 3.3 shows the pseudo-Wigner-Ville distribution (with Chebyshev window) of the sum of two chirp signal, given in Equation 3.7.

In Figure 3.3, there are still cross terms, because the windowing function used in Equation 3.24 causes smoothing only in the frequency direction. Therefore, the cross terms in the time direction are not attenuated [20].

3.3.3 Smoothed-Pseudo Wigner-Ville Distribution

In the previous section, we have seen that the pseudo-Wigner-Ville distribution implements smoothing only in the frequency direction. Because of this, the cross terms can not significantly be attenuated by the pseudo-Wigner-Ville distribution. To suppress cross terms in the time direction, *smoothed-pseudo-Wigner-Ville distribution*

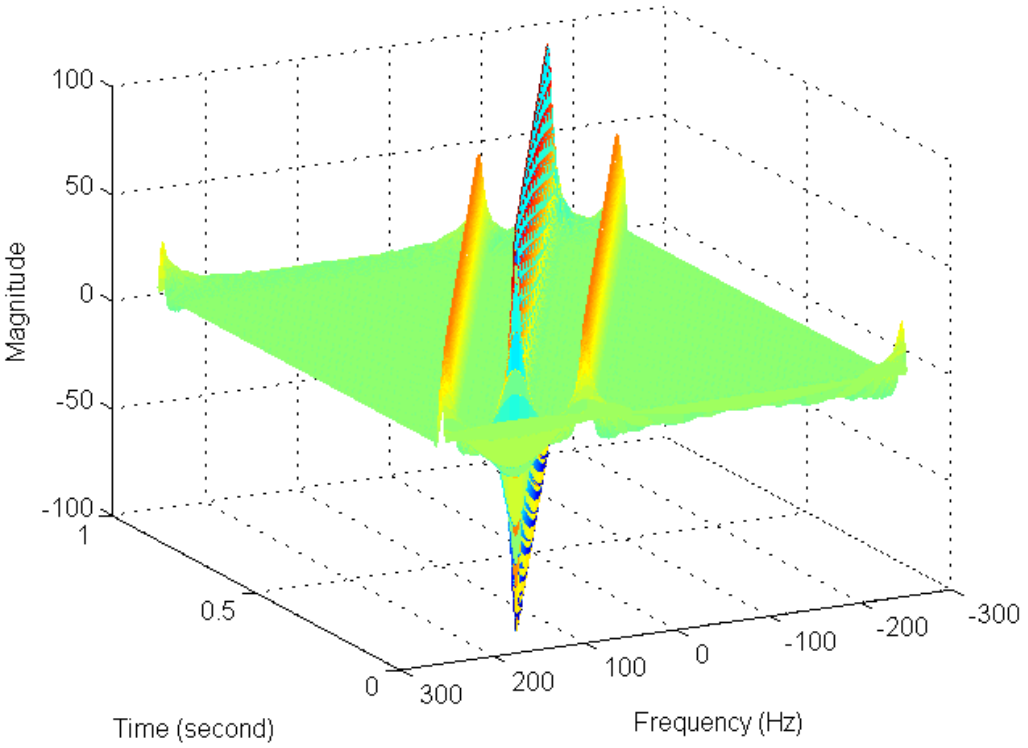

(a) 3-D mesh plot

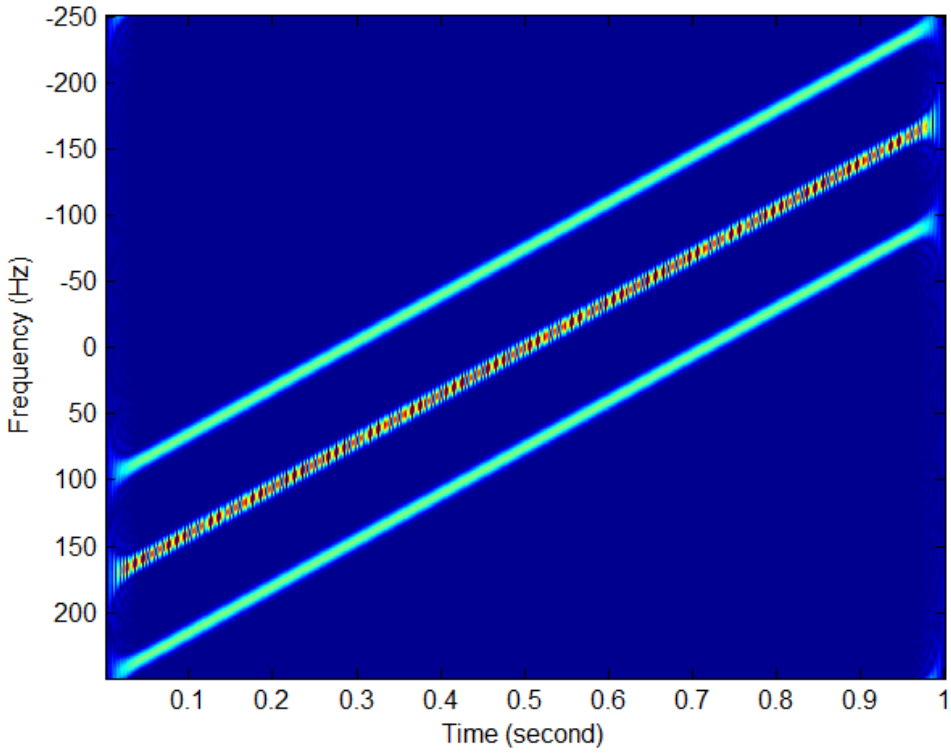

(b) 2-D plot

Figure 3.3: The PWVD of the sum of two chirp with cross term (Equation 3.7).

(SPWVD) is introduced. The smoothed-pseudo-Wigner-Ville distribution is also a pseudo-Wigner-Ville distribution but with an additional smoothing filter in the time direction [20]. If we choose the 2-D smoothing function in Equation 3.20 as

$$\Phi = g(t)H(\omega), \tag{3.25}$$

PWVD becomes SPWVD, where $g(t)$ and $H(\omega)$ (which is the Fourier transform of $h(t)$) are time and frequency windows respectively. Their lengths can be determined independently [21]. A longer $g(t)$ yields more time smoothing and longer $h(t)$ yields less frequency smoothing [20]. Note that choosing $g(t) = \delta(t)$, the SPWVD becomes PWVD with no time smoothing. Equation for the SPWVD can be written as

$$SPWVD(t,\omega) = \int\int WVD(u,\theta)\Phi(t-u,\omega-\theta)dud\theta \tag{3.26}$$

Figure 3.4 shows the smoothed-pseudo-Wigner-Ville distribution of the sum of two chirp signal given by Equation 3.7. As seen from the figure, the cross terms are completely cleared.

3.4 Choi-Williams Distribution

Choi-Williams distribution is a reduced interference distribution with the kernel [22]

$$\phi(\theta,\tau) = e^{-\theta^2\tau^2/\sigma}. \tag{3.27}$$

This kernel function treats like a low pass filter on the $\theta - \tau$ plane. The low pass characteristics of the kernel can be controlled by the constant σ. Larger σ means that more suppression and the smaller σ is less suppression of the cross terms. However, there is a trade of between the suppression of the cross terms and the auto terms. Also note that the kernel converges to the 1 as σ goes to ∞. This means that CWD distribution converges to the WVD as σ goes to ∞. Substituting the kernel in Equation 3.27 into

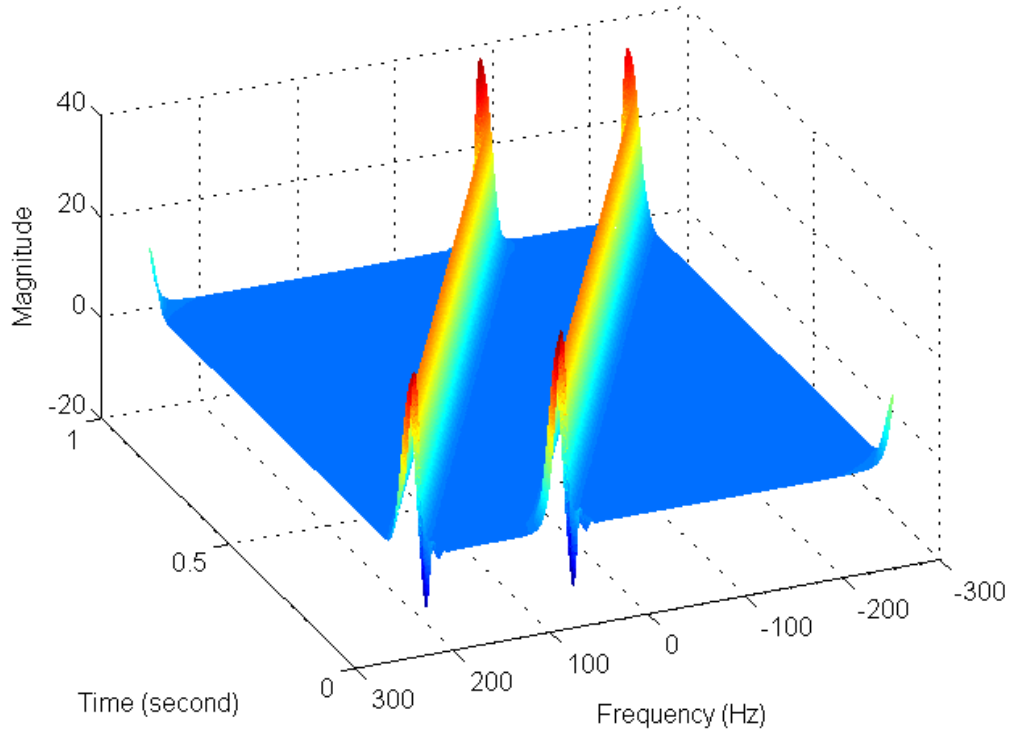

(a) 3-D mesh plot

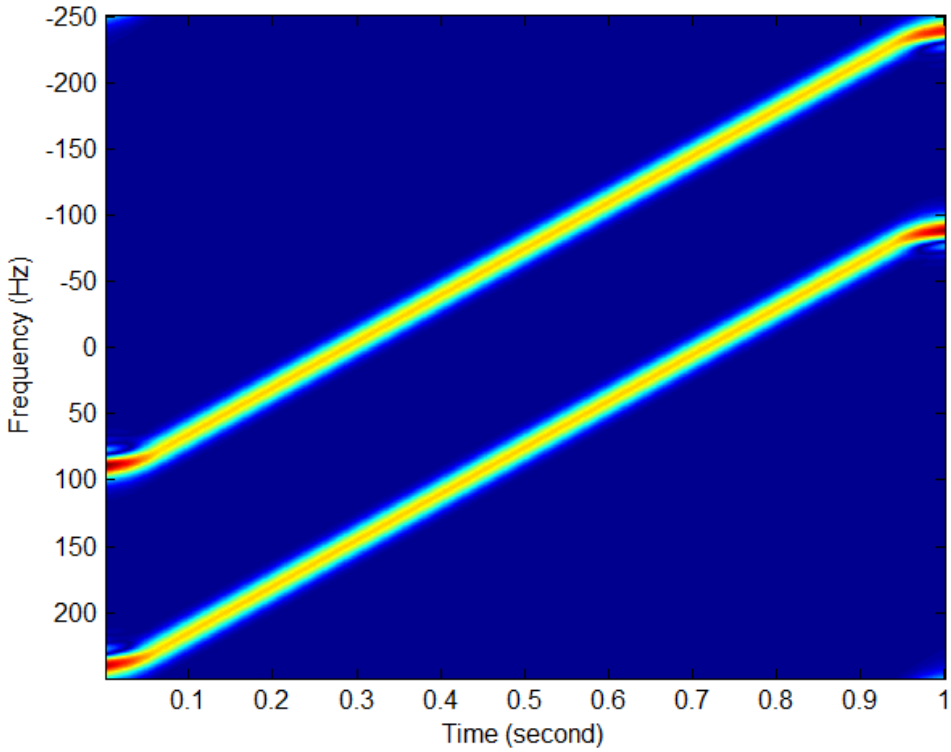

(b) 2-D plot

Figure 3.4: The SPWVD of the sum of two chirp (Equation 3.7).

Equation 3.4, the more general form of Choi-Williams distribution is obtained as

$$CWD(t,\omega) = \frac{1}{4\pi^2}\int\int\int e^{-\theta^2\tau^2/\sigma} s(u+\frac{1}{2}\tau)s^*(u-\frac{1}{2}\tau)e^{-j\theta t - j\tau\omega + j\theta u}dud\tau d\theta. \tag{3.28}$$

Then, by integrating Equation 3.28 over θ, we can obtain

$$\begin{aligned} &CWD(t,\omega) = \\ &\frac{1}{4\pi^{3/2}}\int\int \frac{1}{\sqrt{\tau^2/\sigma}} e^{-\frac{(u-t)^2}{4\tau^2/\sigma}} s(u+\frac{1}{2}\tau)s^*(u-\frac{1}{2}\tau)e^{-j\theta t - j\tau\omega + j\theta u}e^{-j\tau\omega}dud\tau. \end{aligned} \tag{3.29}$$

Figure 3.5 shows the Choi-Williams distribution of sum of two chirp signal given by Equation 3.7. As seen from the figure, the cross terms are completely suppressed from the time-frequency plane.

3.5 Guo-Durand-Lee Distribution

Guo-Durand-Lee distribution (also known as Bessel distribution) is a reduced interference distribution based on the Bessel function of the first kind of order one kernel [23]. Although it is presented to analyze the heart sound and the blood flow signals, it can be used in many applications, because of the high time-frequency resolution and the low cross term level. The kernel for this distribution is defined in the [23] as

$$\phi(\xi,\tau) = \frac{J_1(2\pi\alpha\xi\tau)}{\pi\alpha\xi\tau} \tag{3.30}$$

where ξ is the frequency lag and α is scaling factor. By substituting the kernel given in Equation 3.30 into Equation 3.4 and integrating with respect to ξ (Note that the kernel given in Equation 3.4 is defined based on θ not ξ and $\theta = 2\pi\xi$), we can obtain

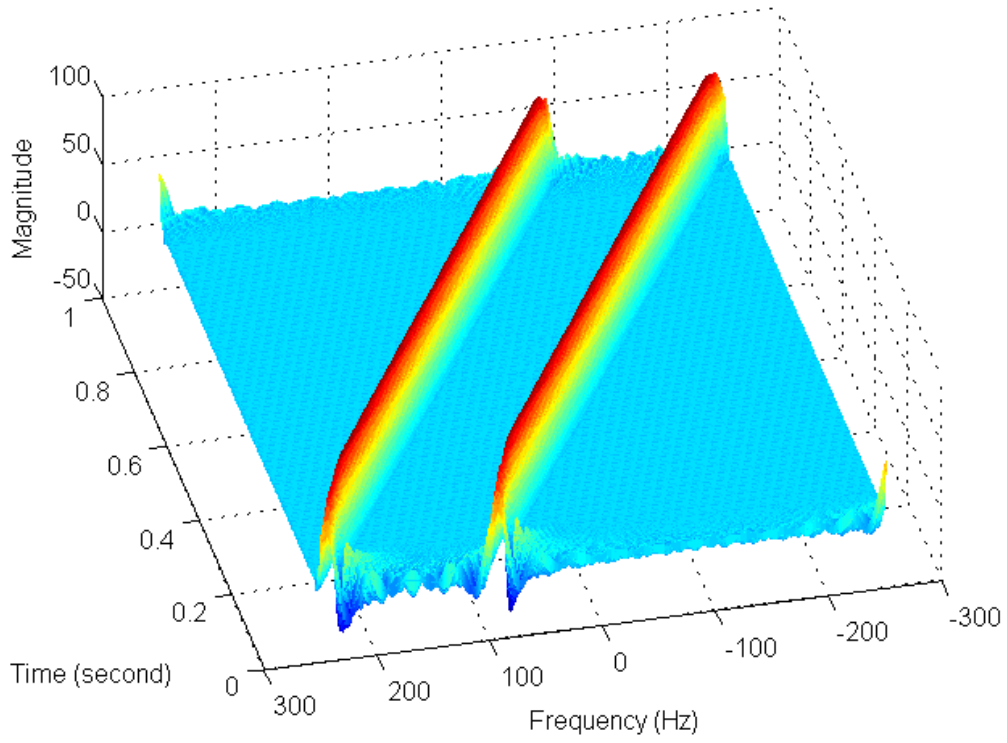

(a) 3-D mesh plot

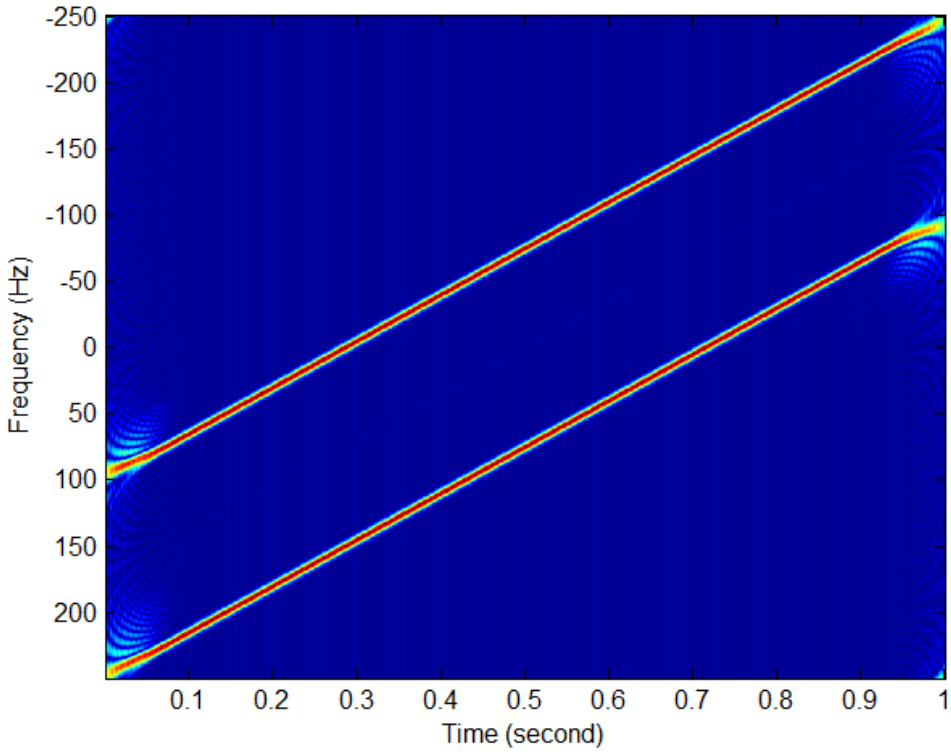

(b) 2-D plot

Figure 3.5: The Choi-Williams distribution of the sum of two chirp (Equation 3.7).

the Guo-Durand-Lee distribution as [23]

$$GDLD(t,\omega) = \int e^{-j\omega\tau}\left[\int \frac{2}{\pi\alpha|\tau|}\sqrt{1-\left(\frac{u-t}{\alpha\tau}\right)^2} \times \Pi(\frac{u-t}{2\alpha\tau})s(u+\frac{1}{2}\tau)s^*(u-\frac{1}{2}\tau)du\right]d\tau \tag{3.31}$$

where

$$\Pi(x) = \begin{cases} 1, & |x| \leq 0.5 \\ 0, & \text{otherwise.} \end{cases} \tag{3.32}$$

The rectangular function Π is used to block the negative values under square root function.

Figure 3.6 shows the Guo-Durand-Lee distribution of sum of two chirp signal given in Equation 3.7. As seen from the figure, the cross terms are completely cleared from the time-frequency plane.

3.6 Cubic Phase Function

The cubic phase function is defined as

$$CP(t,\Omega) = \int_0^\infty s(t+\tau)s(t-\tau)e^{-j\Omega\tau^2}d\tau \tag{3.33}$$

where Ω is the instantaneous frequency rate for the spectrum of cubic phase function [35] [36].

The cubic phase function is a bilinear time-frequency rate distribution function. It has a similar form to the Cohen's class time frequency distributions. However, the cubic phase function is used to estimate the instantaneous frequency rate of the signal. Consider the cubic phase signal

$$s(t) = Ae^{j(a_0+a_1t+a_2t^2+a_3t^3)}. \tag{3.34}$$

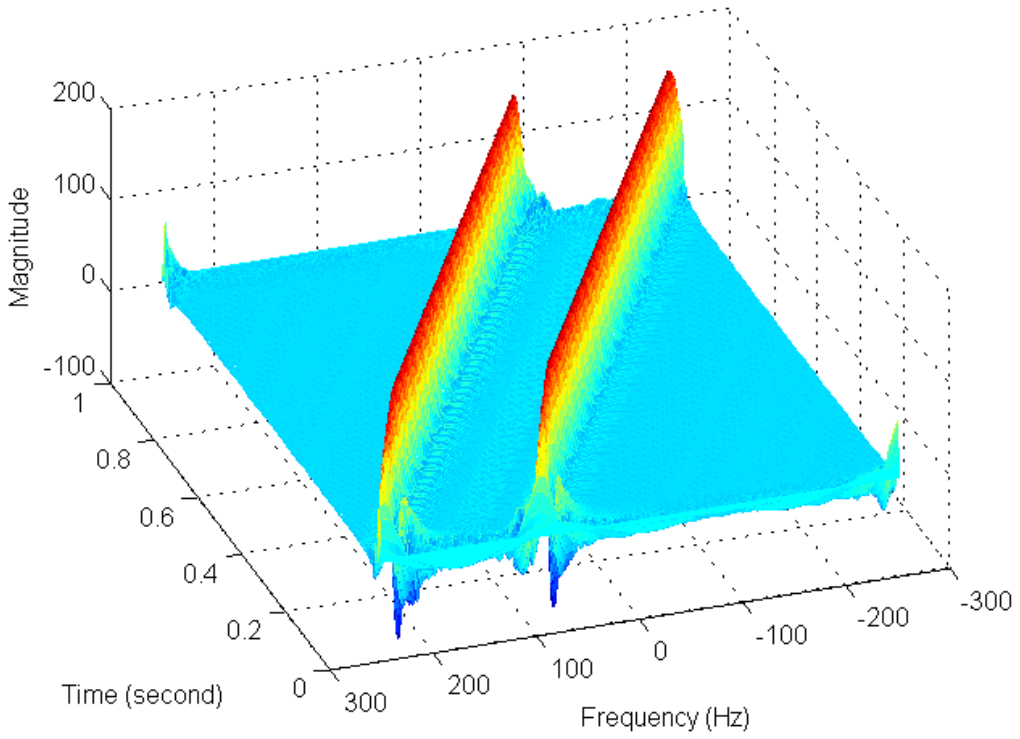

(a) 3-D mesh plot

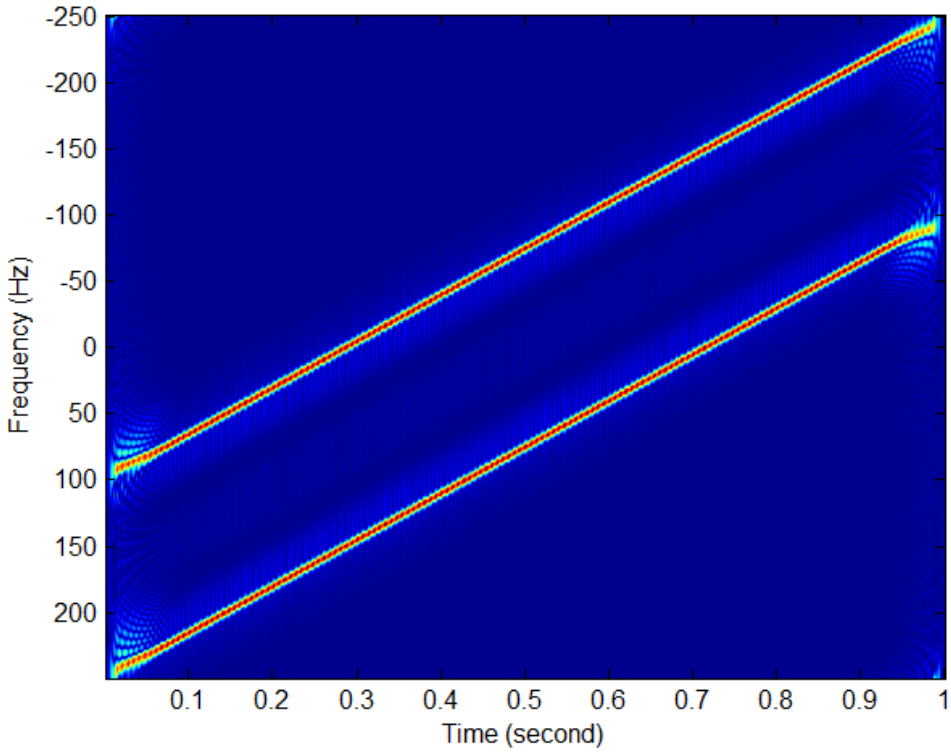

(b) 2-D plot

Figure 3.6: The Guo-Durand-Lee distribution of the sum of two chirp (Equation 3.7).

By substituting $s(t)$ given in Equation 3.34 into Equation 3.33, one can obtain

$$\begin{aligned} &CP(t,\Omega) \\ &= \int_0^\infty Ae^{j(a_0+a_1(t+\tau)+a_2(t+\tau)^2+a_3(t+\tau)^3)} Ae^{j(a_0+a_1(t-\tau)+a_2(t-\tau)^2+a_3(t-\tau)^3)} e^{-j\Omega\tau^2} d\tau \\ &= A^2 e^{j(2a_0+2a_1t+2a_2t^2+2a_3t^3)} \int_0^\infty e^{(2a_2+6a_3t-\Omega)\tau^2} d\tau. \end{aligned} \tag{3.35}$$

The Equation above gives distribution of power on the time-frequency rate plane for $s(t)$. It is obvious that the peaks of the distribution lies on the line $\Omega = 2a_2 + 6a_3t$. Instantaneous frequency rate is defined as the second derivative of the phase of the signal. The frequency rate of the signal given in Equation 3.34 is

$$\begin{aligned} IFR &= \frac{d^2(a_0 + a_1t + a_2t^2 + a_3t^3)}{dt^2} \\ &= 2a_2 + 6a_3. \end{aligned} \tag{3.36}$$

which is equal to the peak curve of the cubic phase function.

Figure 3.7 shows the cubic phase time-frequency rate distribution of sum of two cubic phase signals, $\exp(j2pi(500+50t+25t^2+75t^3))+\exp(j2pi(500+50t+25t^2+100t^3))$. Frequency rate curves of the signals are calculated as $50 + 450t$ Hz/sec and $50 + 600t$ Hz/sec respectively. The calculated curves can easily be seen from the Figure 3.7a and Figure 3.7a.

Due to its bilinear structure, for multicomponent signals, cubic phase function suffers from cross terms [37] [38] [39]. Another handicap of cubic phase function is that if the phase order of the signal is higher than 3, the cubic phase function is biased and inner interferences occurs [38]. For example, for 4^{th} order polynomial phase signal, the cubic phase function peaks along the $2a_2 + 6a_3t + 2a_4\tau^2 + 12a_4t^2$, which depends on the delay term. Therefore, the peaks of the cubic phase function is no more a line. Because of these reasons, the cubic phase function is not applicable to the blade return signal to get time-frequency rate distribution, which has sinusoidal phase.

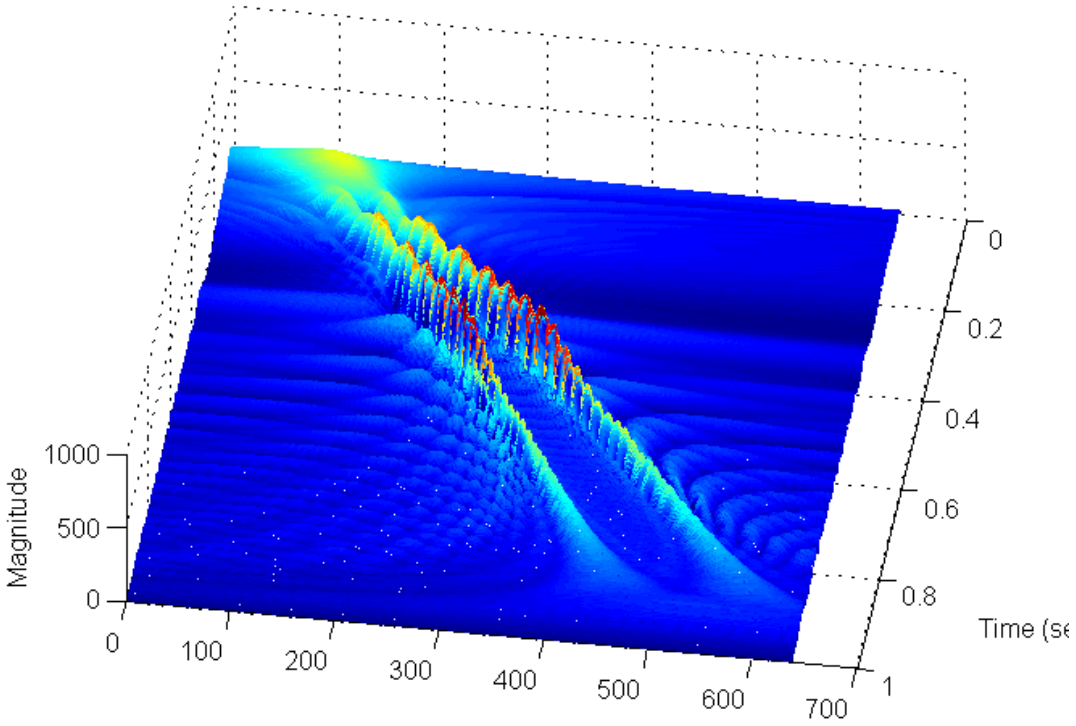

(a) 3-D mesh plot

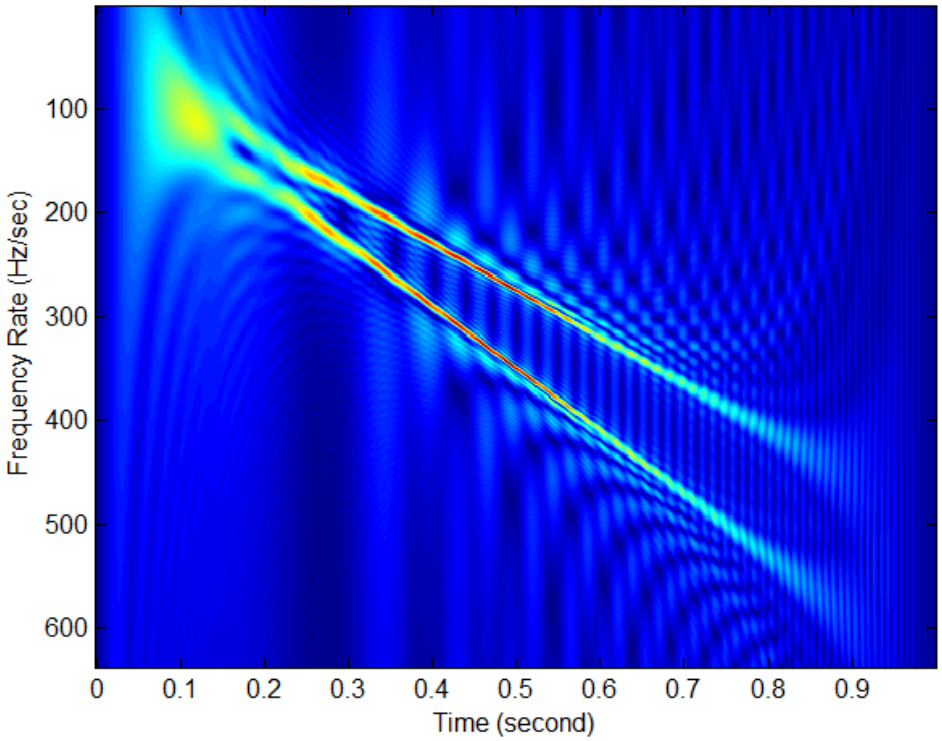

(b) 2-D plot

Figure 3.7: The Cubic Phase Function of the sum of two cubic phase signal.

CHAPTER 4

PROPOSED ALGORITHM

This chapter describes the signal processing algorithm that can be used to extract blade parameters from simulated blade return signal. Firstly, the return signal will be analyzed with traditional methods. Then, the proposed algorithm will be described.

4.1 Introduction

To identify a target, the target must have different features that others do not have. For a helicopter, most characteristic part is blade and the most distinctive blade parameters are number of blades and blade length. The table below shows the different blade parameters for different type of helicopters.

Table 4.1: Blade Parameters for Different Helicopters

Helicopter	**Blade Length (m)**	**Num. of Blades**	**Max rps**
AH-1W SUPERCOBRA	7.3	2	4.9
BELL-206 LONGRANGER	5.64	2	6.5
EC-130 EUROCOPTER	5.35	3	6.5
EC-120 COLIBRI	5	3	6.9
AH-64 APACHE	7.3	4	4.8
UH-60 BLACK HAWK	8.18	4	4.3
MD-500	4.02	5	8.2
CH-53 SEA STALLION	11	6	3.1
CH-53E SUPER STALLION	12.04	7	2.9

As seen from Table 4.1, helicopters can be identified by their blade lengths and number of blades. The proposed method tries to extract these parameters. The algorithm starts with getting time-frequency image of the helicopter blade signal. After get-

ting the image, the flash times and positions of the approaching and receding blades will be found separately. Then, the tip Doppler frequency of the blades will be estimated. At the end, the Hough transform will be implemented on the time-frequency image with the parameters found before in order to estimate the period of blade tip modulation.

In this chapter, the helicopters used in simulations are *AH-64 APACHE* and *EC-130 EUROCOPTER*. The rotation rate of the blades are 4.8 and 6.5 rps respectively (max rps values are used). The blade numbers and the blade lengths are given in the Table 4.1.

For this work, the used radar is a pulsed Doppler tracking radar. Assume that tracking is perfect such that the target is always in the 3 dB beamwidth of the radar and the returned pulse from the target is always in the range gate of the radar. The radar has also the capability to track the helicopter fuselage Doppler frequency. The COHO (coherent oscillator) is operated by the output of the Doppler tracker in order to set the helicopter fuselage return signal's frequency to exactly middle of the IF (intermediate frequency). After that, a perfect MTI (moving target indicator) circuit suppresses the fuselage signal. Therefore, only remaining signal component is the blade return. Because of this reason, in this work, only the blade return signal at the baseband is modeled.

The effective parameters of the radar for our algorithm are the carrier frequency and the prf (pulse repetition frequency). As given in Equation 2.10, the received Doppler frequency is directly depended on the carrier frequency of transmitted signal.

The prf value is the sampling rate of target motion. To get alias free spectrum (or spectrogram), the prf value must be at least twice the maximum Doppler frequency. The maximum received Doppler frequency is the blade tip Doppler frequency when the blade is perpendicular to radar line of sight. The linear velocity of the blade tip is

$$V_{tip} = 2\pi L f_{rotor} \tag{4.1}$$

Main rotor blades are designed to have a maximum linear tip velocity which is less than the speed of sound (about 340 m/s). Therefore the maximum tip Doppler fre-

quency according to Equation 2.14 is 22.67 kHz. The prf is twice of the maximum Doppler frequency, which is about 45.3 kHz. However, for bilinear time-frequency distributions, the sampling frequency must be twice the Nyquist rate [10], which is 90.6 kHz. Therefore, the 90 kHz prf is chosen for simulations.

In this chapter, for the simplicity of understanding of the algorithm, the noise power is chosen as 60 dB below the ***peak*** power (occurs when one of the blades is perpendicular to the radar line of sight) of the received signal (PSNR = 60 dB).

In this work, returned blade signal from helicopter is modeled as described in Chapter-2. Contribution of tail rotor is ignored since the main rotor blades have larger RCS than tail rotor blades, and the returned Doppler frequency of tail rotor is generally much higher than the Doppler frequency caused by the main rotor [25]. It is also assumed that while the observation time, the rps of the main rotor stays constant.

4.2 SNR Anaylsis

There are two noise sources for radar receivers. First one is the receiver thermal noise caused by wave guides, duplexers, amplifiers and other receiver parts. The second noise source is the noise that comes from the environment. In the calculations in this work, this noise source is not considered. The noise is created with the desired SNR value which is defined as

$$SNR = \frac{P_s}{P_n} \tag{4.2}$$

where P_s is the signal power and P_n is the additive noise power. The noise is modeled as complex Gaussian random variables with variance of σ^2. The power of the noise (P_n) is the variance (σ^2) of it. Therefore, the generated noise is

$$\mathcal{CN}(0, \frac{P_s}{SNR}). \tag{4.3}$$

However, the signal returned from the helicopter blades is not constant. As seen from Figure 4.2 and Figure 4.3, the ratio of maximum and minimum received powers is

about 55 dB. Note that the receiver thermal noise level stays constant. Therefore, for this situation, the SNR must be defined in a different manner. One way is using PSNR (Peak Signal-to-Noise ratio). The peaks signal level is received when one of the blades is perpendicular to the radar line of sight. This means that the ωt term in Equation 2.29 is equal to $\pi/2$ (or $-\pi/2$). The another way to express the SNR is average SNR, which is the ratio of average received power to average noise power in a period of time. Average received power can be calculated by using

$$P_{s,average} = \frac{1}{N} \sum_{n=1}^{N} |s[n]|^2 \tag{4.4}$$

where $s[n]$ is the sampled received signal (sampled with pri) and N is the total number of received pulses such that,

$$N = \frac{1}{f_{rotor} \times pri}. \tag{4.5}$$

Note that $1/f_{rotor}$ is one period of helicopter rotor, therefore N is the total number of received pulses within one period. The summation is from 1 to N, because the returned signal from blades is periodic with a period of $1/f_{rotor}$.

Variation of SNR in time can be seen from Figure 4.1a and Figure 4.1b. The figures are obtained for 60 dB PSNR values. The calculated average SNR values are 28.28 dB and 34.24 dB respectively. Note that although the PSNR values are same, there is a difference between the average SNR values. One reason is that while AH-64 APACHE has 4 blades (even number), the EC-130 has 3 blades (odd number). For even number blade returns, the flashes are caused by two blades. Another reason of the difference is the blade length. A flash resulting from a longer blade length will have a shorter duration while for a shorter blade, it will spread over time [24].

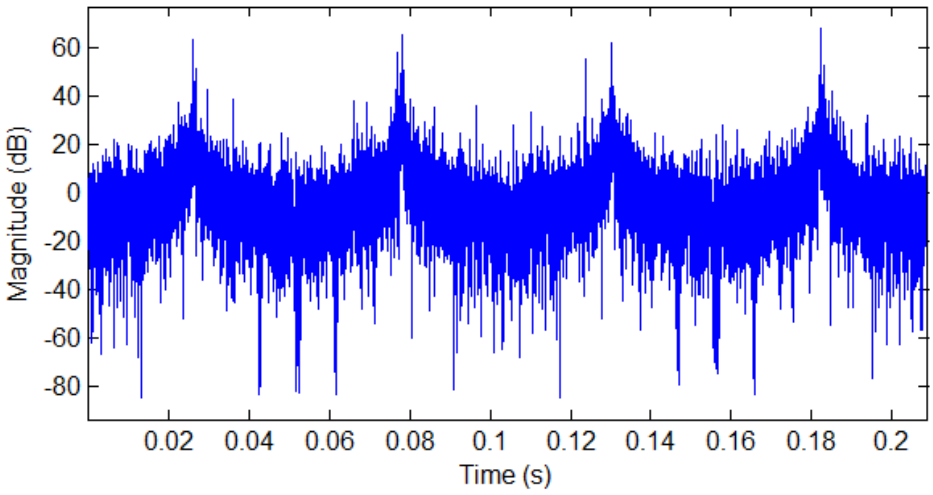

(a) AH-64 APACHE

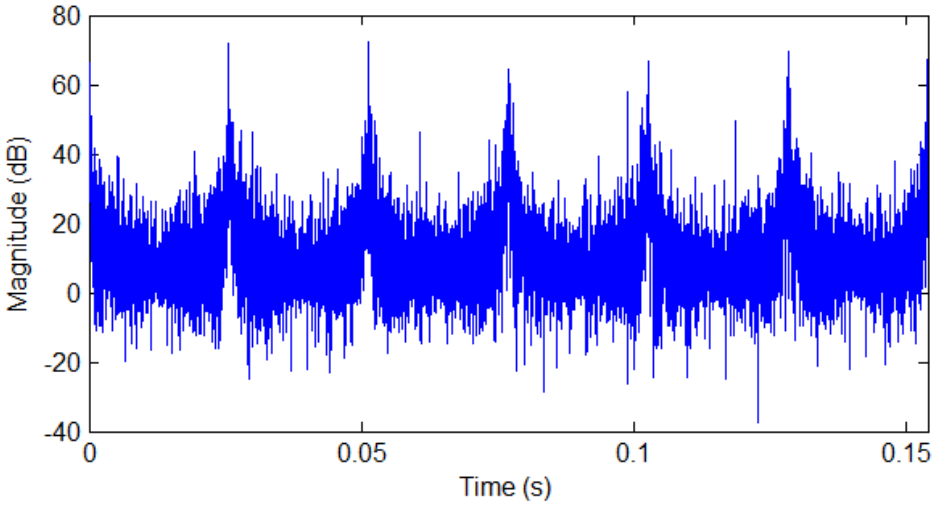

(b) EC-130

Figure 4.1: SNR versus Time (for 60 dB PSNR).

4.3 Return Signal Analysis

The returned signals from blades of helicopter is modeled as described in Chapter-2. The resultant received signal for AH-64 APACHE is shown in Figure 4.2. The blade flashes can easily be recognizable from the figure. Remember that the flashes occur when a blade is oriented perpendicular to the radar line-of-sight at which the RCS is maximum. Because there are even number of blades, two of the blades are oriented perpendicular to the radar line of sight simultaneously. There are four flashes, because

the observation time is equal to one period of main rotor which is $1/4.8 = 0.2083$ s. The received signal from the blades of EC-130 is shown in Figure 4.3. There are 6 flashes seen throughout one period of the helicopter rotor. The reason why there are $2\times$(number of blades) flashes is that there are odd number of blades. Therefore, there is no overlapping between the approaching and receding blade flashes.

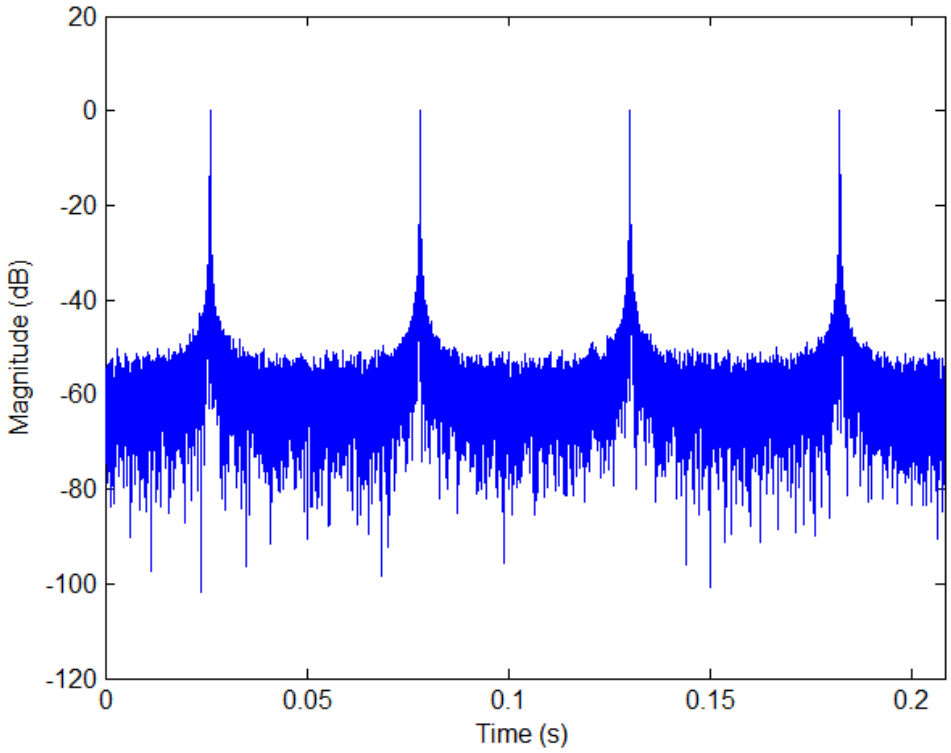

Figure 4.2: Returned Signal Power versus Time (AH-64 APACHE, 4.8 rps).

The observed period of flashes depends on the number of blades n and the main rotor rps as

$$\text{observed period of flashes} = \begin{cases} \frac{1}{2n\times f_{rotor}}, & \text{if n is odd} \\ \frac{1}{n\times f_{rotor}}, & \text{if n is even} \end{cases} \tag{4.6}$$

which is the only information extracted from the time signal.

Fourier transform of the returned signal can be seen in Figure 4.4. The positive Doppler side of the plateau region is caused by approaching blade returns while negative side is caused by the receding blade returns. The tip velocity of the helicopter

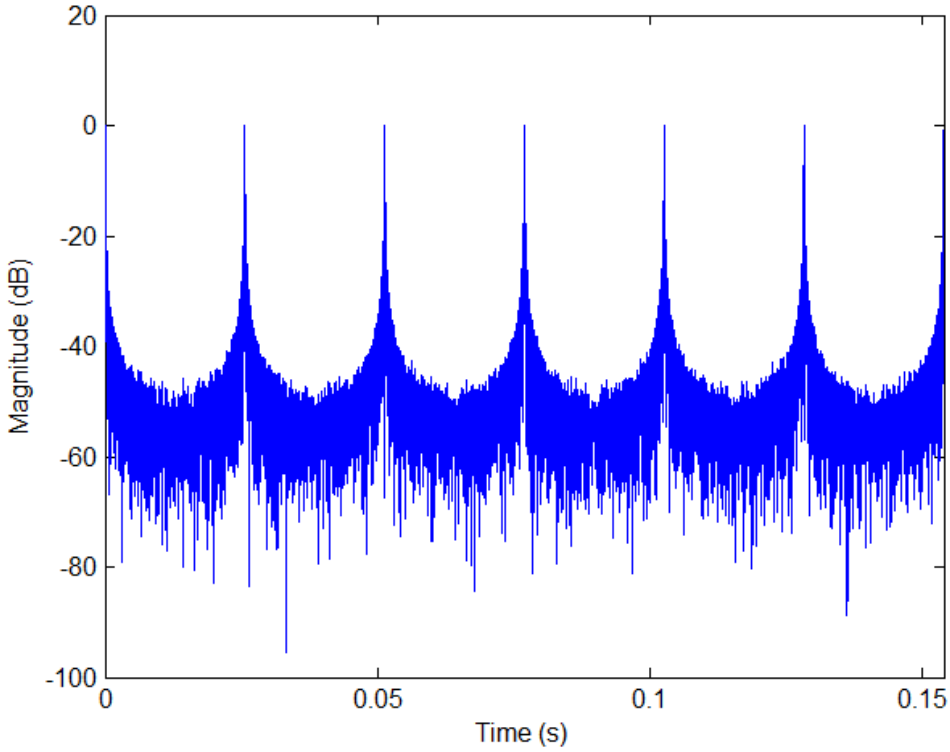

Figure 4.3: Returned Signal Power versus Time (EC-130, 6.5 rps).

blade is calculated as ∼220.16 m/s by using Equation 4.1. The corresponding maximum tip Doppler frequency is the 14.677 kHz which can be verified from Figure 4.4. The spectrum of received signal from the EC-130 can be seen in Figure 4.5. The tip velocity of the blades of EC-130 is 218.5 m/s. The corresponding maximum tip Doppler frequency is 14.566 kHz. This can be seen from the spectrum of EC-130 in Figure 4.5.

Note that the maximum tip Doppler frequency is not a useful information alone, but it gives the information about L $\times$ f_{rotor}. By solving Equation 4.1 into Equation 2.14, it gives

$$F_{D,tip} = \frac{2 \times 2\pi L f_{rotor}}{\lambda}. \tag{4.7}$$

The analysis given in this section shows that the signal and the frequency spectrum of the blade return are not sufficient to extract the necessary parameters for helicopter identification. Therefore, more detailed analysis needed.

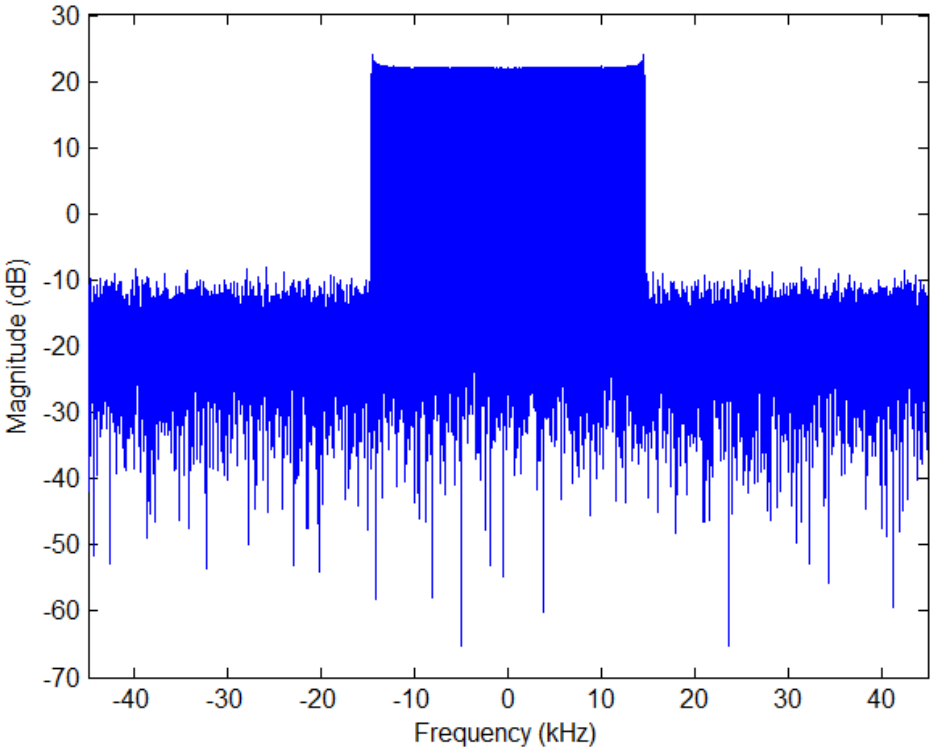

Figure 4.4: Returned Signal Spectrum (AH-64 APACHE, 4.8 rps).

4.4 Parameter Extraction Using Joint Time-Frequency Analysis

The analysis in the previous section shows that the traditional analysis of time and frequency is not sufficient for helicopter blade parameter estimation. Therefore, joint time-frequency techniques are used for parameter extraction. One advantage of joint time-frequency analysis is that one can separate the flashes due to approaching or receding blades. This can not be possible using time signal or spectrum. In time signal, the flash instants can easily be seen but there is no way to understand if it is caused by an approaching or receding blade. While spectrum shows the power of each frequency component of the return signal, there is no information about when that frequency occurred. Another advantage is that it allows to observe the trace produced by the tip of the blades. In this chapter, the time-frequency distribution of the return signal is obtained using smoothed pseudo Wigner-Ville distribution.

Figure 4.6 shows the SPWVD of the returned signal of AH-64 APACHE. As seen from the figure, the Doppler frequency of the flashes are both negative and positive,

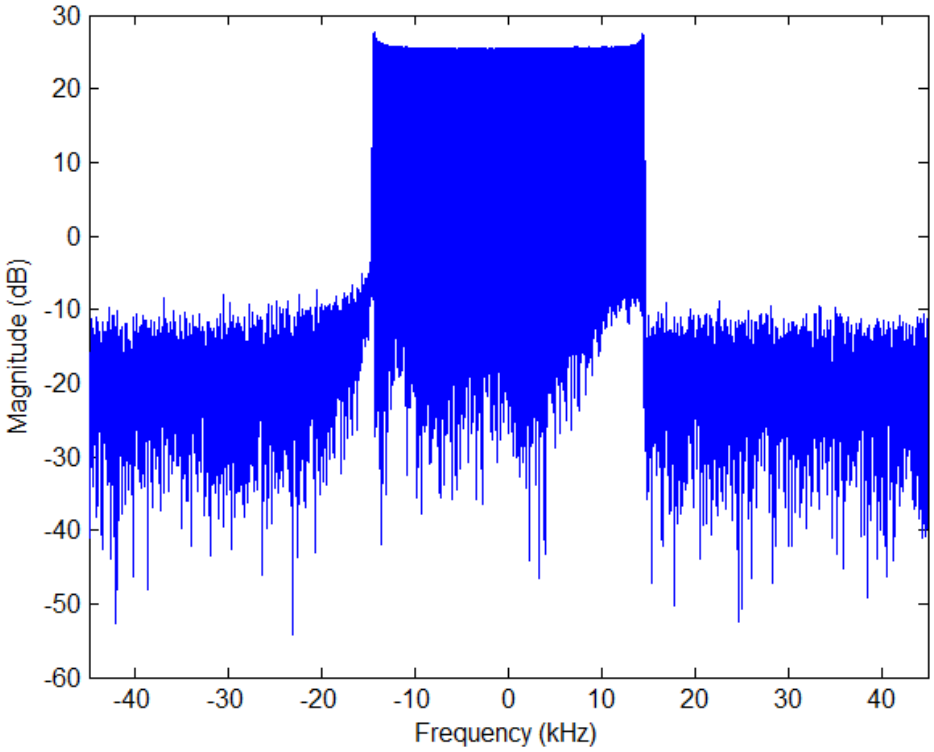

Figure 4.5: Returned Signal Spectrum (EC-130, 6.5 rps).

because two of the blades are oriented perpendicular to the radar line of sight simultaneously. It can also be seen that the tips of the blades produce sinusoidal traces [3].

Figure 4.7 shows the SPWVD of the returned signal of EC-130 with 6.5 rps. As seen from the figure, the flashes have positive frequencies and negative frequencies occurring at different times. Since there are odd number of blades, the approaching and receding blade flash times are different.

As seen from Figure 4.6 and Figure 4.7, the flash periods can be calculated separately for approaching and receding blades. It is an important parameter for the blade feature extraction as seen from Equation 4.8.

$$T_{flash,approaching} = T_{flash,receding} = \frac{1}{n \times f_{rotor}}. \tag{4.8}$$

Note that the period of approaching and receding blades are equal. because of this reason, both can be called as T_{flash}. With joint time-frequency analysis, we can get

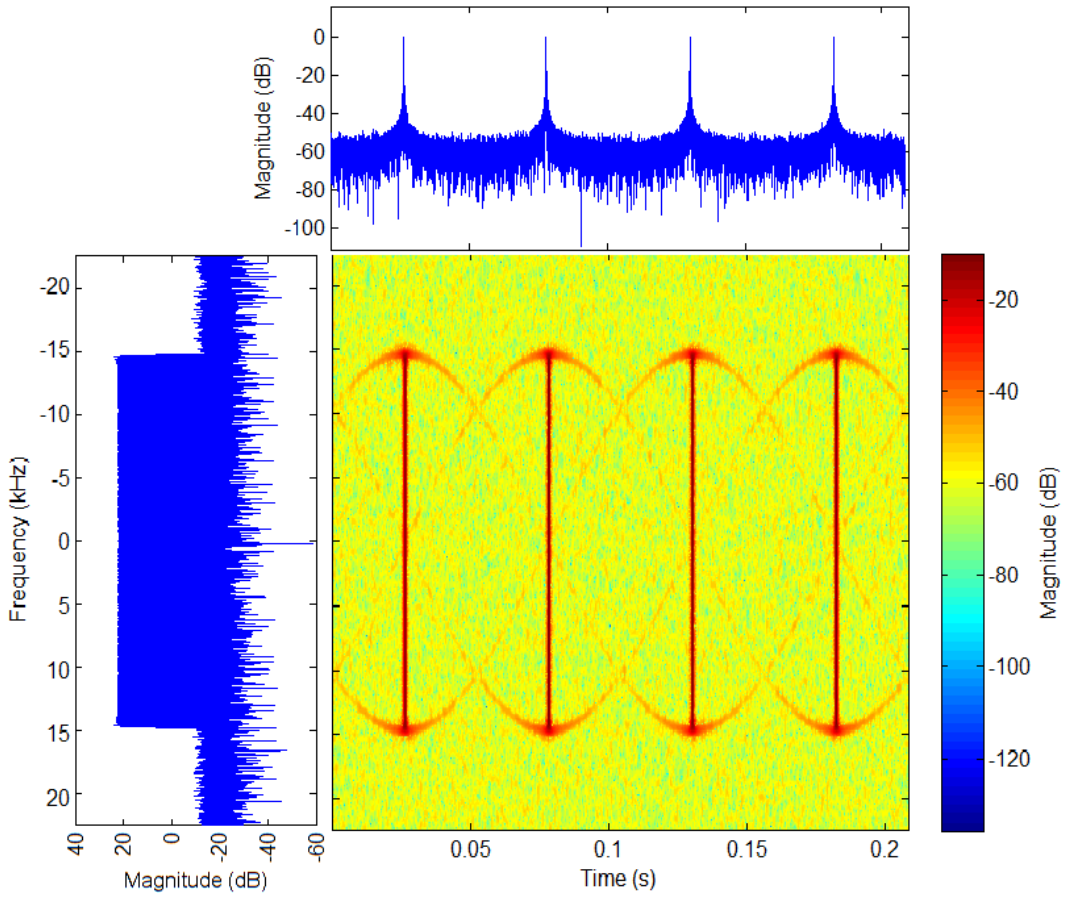

Figure 4.6: SPWVD of Returned Signal (AH-64 APACHE, 4.8 rps).

the information about if there are even or odd number of blades. Therefore, it is more useful to use the T_{flash} instead of the observed flash period measured from the time signal. The Equation 4.8 is the modified version of Equation 4.6 with separately extracted information about approaching and receding blade periods.

As seen from Equation 4.6, without blade tip trace, the obtained informations are still insufficient to calculate number of blades. We also need to extract the rps (or period) of blades. The information about the rps of blades can be extracted from the time-frequency image. The sinusoidal trace of blade tips gives the angular information about the blades. The period of traces equals to $1/f_{rotor}$. Note that each trace has same period. As seen from Figure 4.6 and Figure 4.7, the periods of tip traces are about $\sim$0.208 ms and $\sim$0.154 ms respectively, which corresponds to

$$T_{\text{tip trace}} = 1/f_{rotor}. \tag{4.9}$$

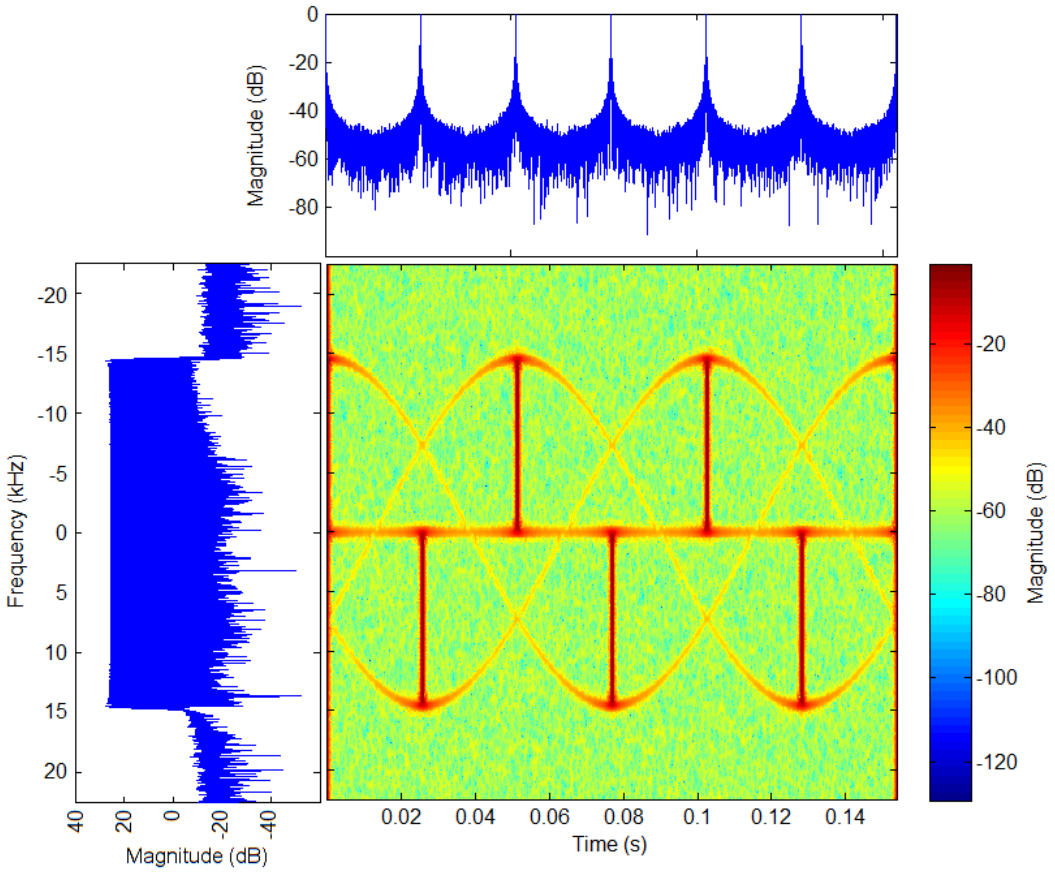

Figure 4.7: SPWVD of Returned Signal (EC-130, 6.5 rps).

Now there are two equations (Equation 4.8 and Equation 4.9) with two unknowns (f_{rotor} and n). Therefore, one of the blade parameters, number of blades, can be calculated as

$$n = \frac{T_{\text{tip trace}}}{T_{flash}}. \tag{4.10}$$

Another parameter of the blade is the length of the blade. To obtain an equation for the blade length, Equation 4.9 can be solved into Equation 4.7. The resultant equation is

$$L = \frac{F_{D,tip}\lambda T_{\text{tip trace}}}{4\pi} \tag{4.11}$$

Therefore, for the estimation of blade parameters, n and L, the required measurements are T_{flash}, $F_{D,tip}$ and $T_{\text{tip trace}}$.

4.4.1 Finding Flash Period (T_{flash})

The period of approaching and receding blades (T_{flash}) can be calculated by finding the approaching and receding flash instances in the time-frequency image. The main reason of why we could not use time domain signal to find flash instances is that there is no information about if the flash is from an approaching or receding blade. However, magnitude square of time signal can be separated into two parts such that each part has desired Doppler, as

$$|s(t)|^2 = |s_+(t)|^2 + |s_-(t)|^2 \tag{4.12}$$

where $s_+(t)$ is the positive Doppler frequency component and the $s_-(t)$ is the negative Doppler frequency component. Note that magnitude square of time signal gives instantaneous power. As seen from Figure 4.6 and Figure 4.7, the approaching flashes are at the positive frequency side of the time frequency image while receding flashes are at the negative frequency side. Therefore, the positive frequency side of the time-frequency distribution image is the time-frequency distribution of the $s_+(t)$ and the negative side of it is the time-frequency distribution of the $s_-(t)$. However, the problem is getting the time signal from the time-frequency distribution. Remember that the time marginal property of the ideal joint time-frequency distribution given in Equation 3.2, summing up the energy distribution for all frequencies at a particular time gives the instantaneous power of the signal at that time. Therefore,

$$|s(t)_+|^2 = \int_0^{+\infty} P(t,\omega)d\omega \tag{4.13}$$

and

$$|s(t)_-|^2 = \int_{-\infty}^{0} P(t,\omega)d\omega \tag{4.14}$$

where $P(t,\omega)$ is the joint-time frequency distribution. Figure 4.8 and Figure 4.9 show the positive and negative Doppler sides of SPWVD of $s(t)$ and the obtained $|s_+(t)|^2$ and $|s_-(t)|^2$ for the AH-64 APACHE (4.8 rps) and the EC-130 (6.5 rps). Note that

the magnitudes in Figure 4.8a, Figure 4.8b, Figure 4.9a and Figure 4.9b are plotted in linear scale.

4.4.1.1 Noise Analysis And Implementation Of CA-CFAR

To find the flash instances from the time domain signal, CA-CFAR (cell averaging constant false alarm rate) threshold method can be used. If the noise in reference cells are independent and identically distributed samples governed by an exponential distribution, the CA-CFAR detector is nearly optimal (as number of reference cell increases, the detector approaches to optimum detector) [26].

The basic idea of CA-CFAR is to calculate an adaptive threshold level for the changing conditions instead of determining a hard threshold level. The detector adjusts the threshold level with desired and measured parameters. The desired parameter is probability of false alarm, and the measured parameter is the mean power of the noise (or interference). The actual average interference power is estimated from the signal and so the threshold level is continuously adjusted to provide the desired false alarm rate. This type of detectors is called as CA-CFAR.

Block diagram of CA-CFAR detector can be seen in Figure 4.10. There is a sliding window that contains reference cells, guard cells and the cell under test (CUT). The reference cells are used to calculate the average interference power. The CUT is tested if it exceeds the calculated threshold or not. The CUT and the guard cells are not taken into account while calculating the average interference power.

The average interference power can be calculated as

$$Z = \frac{1}{M} \sum_{i=1}^{M} x_i \tag{4.15}$$

where x_i is the power at the i^{th} reference cell and M is the total number of reference cells. The threshold multiplier K_0 is calculated as

$$K_0 = M(pfa^{-1/M} - 1) \tag{4.16}$$

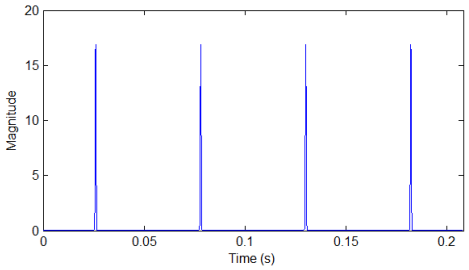

(a) $|s_+(t)|^2$

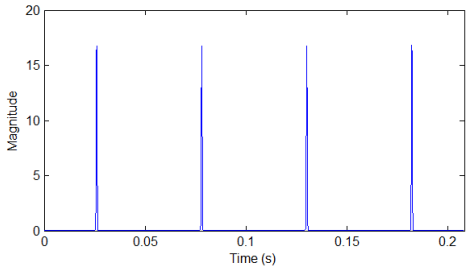

(b) $|s_-(t)|^2$

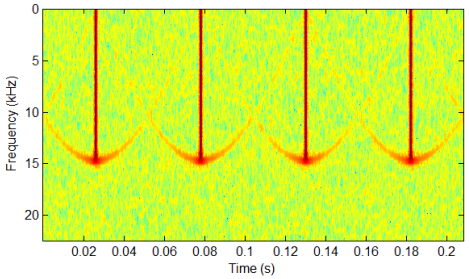

(c) Positive Doppler Side of SPWVD of $s(t)$

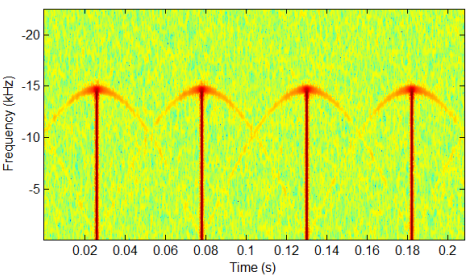

(d) Negative Doppler Side of SPWVD of $s(t)$

Figure 4.8: The Positive and Negative Doppler Sides of SPWVD of $s(t)$ and the Obtained $|s_+(t)|^2$ and $|s_-(t)|^2$ (AH-64 APACHE, 4.8 rps).

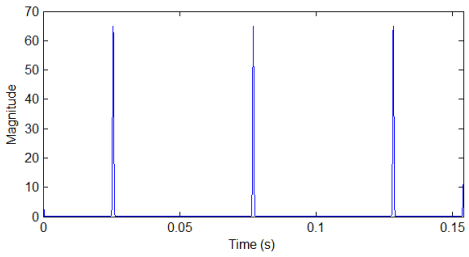

(a) $|s_+(t)|^2$

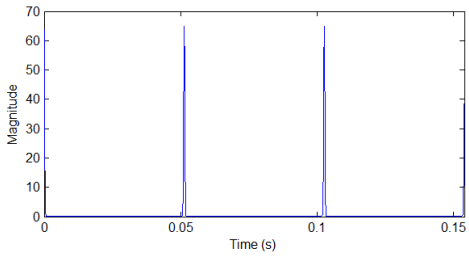

(b) $|s_-(t)|^2$

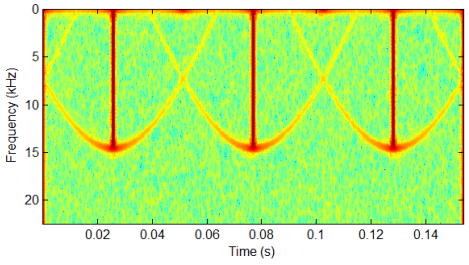

(c) Positive Doppler Side of SPWVD of $s(t)$

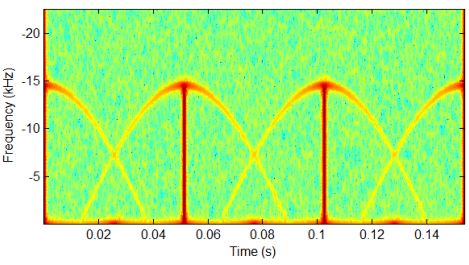

(d) Negative Doppler Side of SPWVD of $s(t)$

Figure 4.9: The Positive and Negative Doppler Sides of SPWVD of $s(t)$ and the Obtained $|s_+(t)|^2$ and $|s_-(t)|^2$ (EC-130, 6.5 rps).

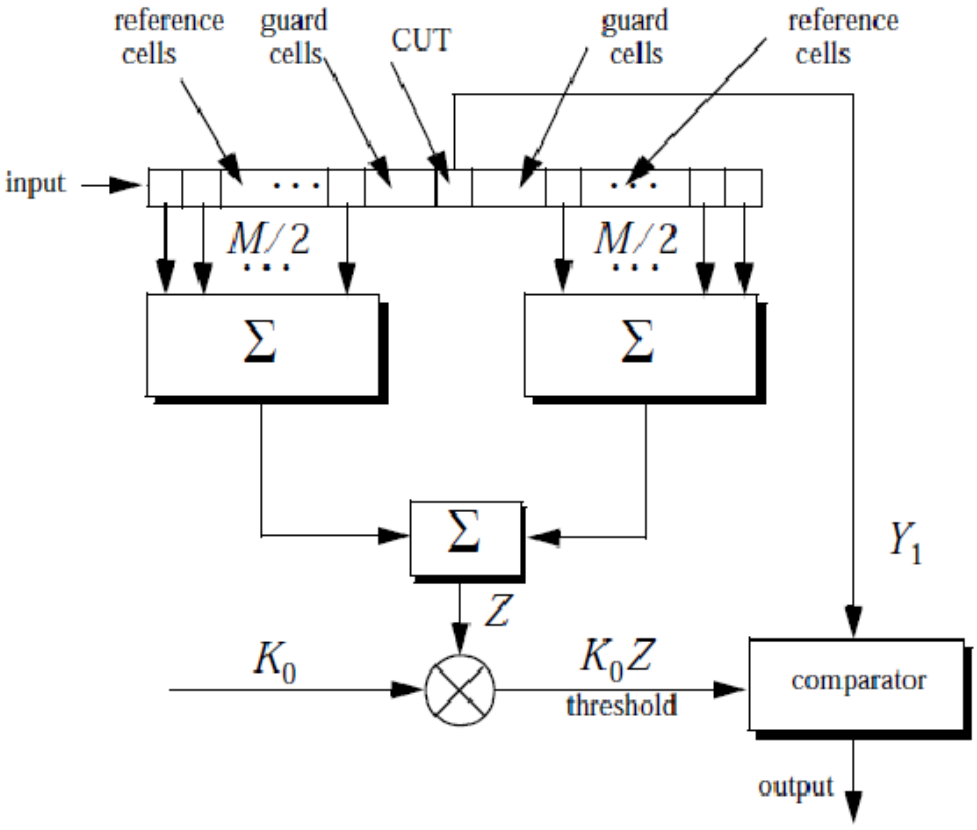

Figure 4.10: Block Diagram of CA-CFAR [29].

where pfa is the probability of false alarm. The resultant threshold level for the CUT is

$$threshold = K_0 Z = (pfa^{-1/M} - 1) \sum_{i=1}^{M} x_i \tag{4.17}$$

However, the noise power distributions of the obtained $|s_+(t)|^2$ and $|s_-(t)|^2$ are not necessarily exponential since many time-frequency distributions do not satisfy the marginal properties. Note that the WVD, CWD and GDLD satisfy the marginals while PWVD, SPWVD and spectrogram do not [23] [27] [28] [20].

Figure 4.11 shows the noise analyses of time signals, which are reverted from the time-frequency distributions by summing up the energy distribution for all frequencies as described in previous section.

Figure 4.11a shows the time domain input signal, which is the generated complex Gaussian noise. Figure 4.11c, Figure 4.11e and Figure 4.11g show the time signal

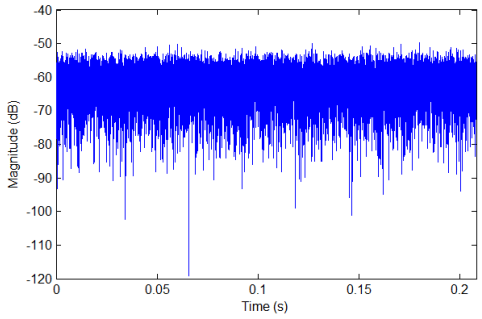

(a) Input Noise

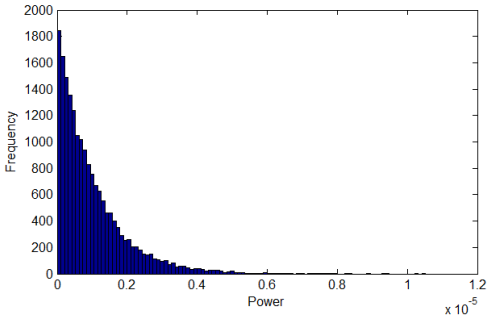

(b) Histogram of Input Noise

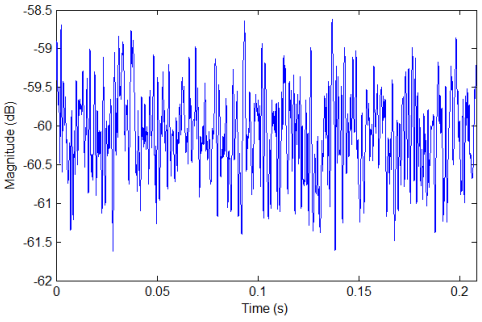

(c) Time Signal Reverted from SPWVD

.

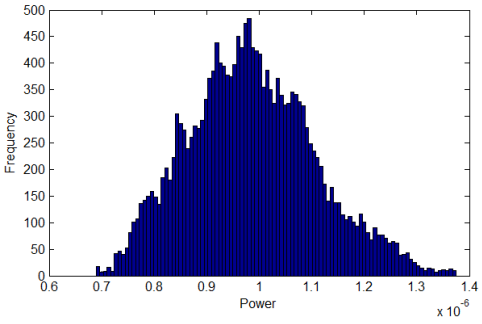

(d) Histogram of Time Signal Reverted from SPWVD

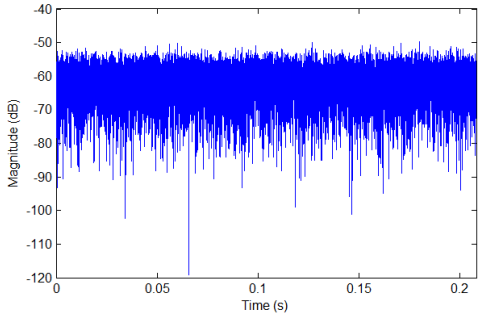

(e) Time Signal Reverted from CWD

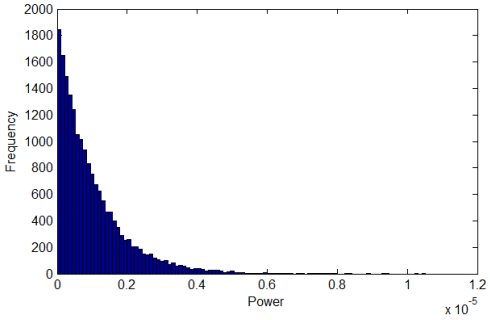

(f) Histogram of Time Signal Reverted from CWD

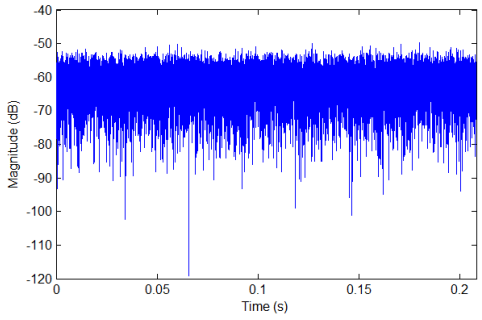

(g) Time Signal Reverted from GDLD

.

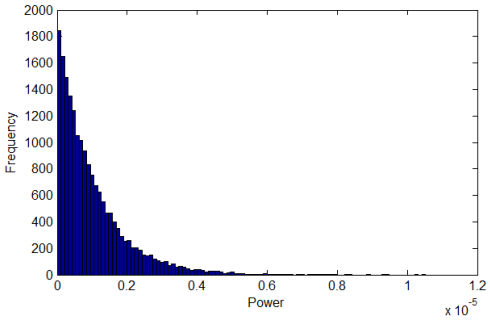

(h) Histogram of Time Signal Reverted from GDLD

Figure 4.11: The Noise analysis in Time-Frequency Distribution.

reverted from SPWVD, CWD and GDLD respectively. Figure 4.11b, Figure 4.11d, 4.11h and Figure 4.11f show the histogram of corresponding signals. As seen from Figure 4.11a, the distribution of the input noise is exponential.

As seen from Figure 4.11c, one can say that, the reverted signal from the SPWVD is different from the original signal which is given in Figure 4.11a. It can easily be recognized that the signal in Figure 4.11c is the smoothed (low-passed) version of the original signal. Also, as seen from the histogram given in Figure 4.11d, the distribution of noise is completely different from the original one which is given in Figure 4.11b. It is an expected result, because the SPWVD does not satisfy the marginal properties.

However, as seen from Figure 4.11e, reverted signal from the CWD is a perfect copy of the original signal given in Figure 4.11a. It is also clear that the distributions of two signals are exactly the same as seen in Figure 4.11f and Figure 4.11b. Similarly, as seen from the Figure 4.11g and 4.11h, the time signal and the histogram are same with the graphs given in Figure 4.11a and Figure 4.11b. This is also expected because, CWD and GDLD satisfy the marginal properties.

Figure 4.12 shows the CA-CFAR implementation over the signals $s_+(t)$ and $s_-(t)$ reverted from the SPWVD for the blade returns of AH-64 APACHE and EC-130. For the simulations, the probability of false alarm (pfa) is set to 10^{-5}. As seen from the graphs, the CA-CFAR threshold is exceeded at flash instances.

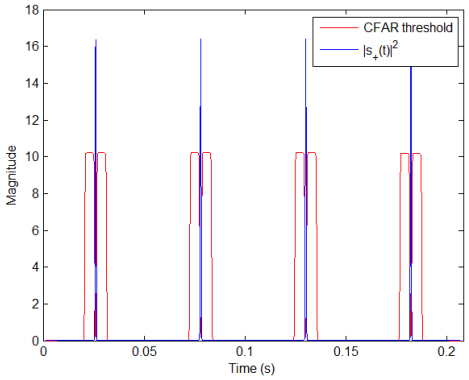

(a) $|s_+(t)|^2$ and the Calculated CFAR Threshold (AH-64 APACHE, 4.8 rps)

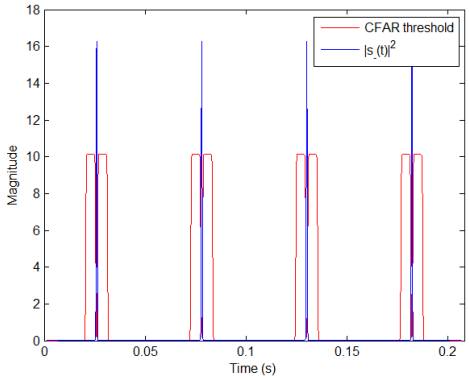

(b) $|s_-(t)|^2$ and the Calculated CFAR Threshold (AH-64 APACHE, 4.8 rps)

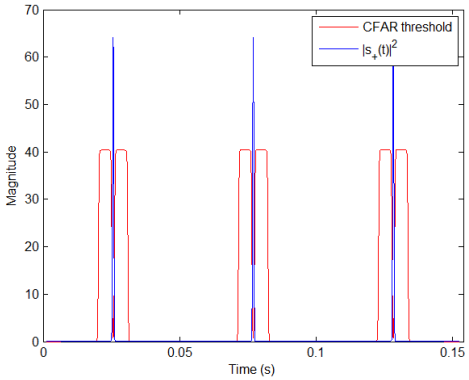

(c) $|s_+(t)|^2$ and the Calculated CFAR Threshold (EC-130, 6.5 rps)

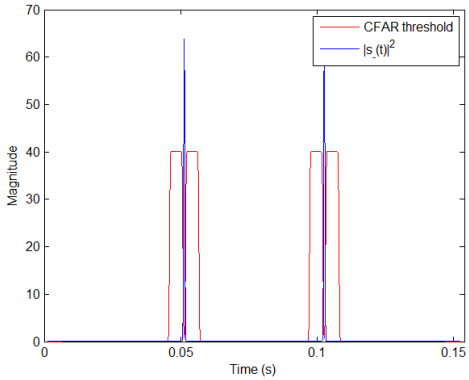

(d) $|s_-(t)|^2$ and the Calculated CFAR Threshold (EC-130, 6.5 rps)

Figure 4.12: Implementation of CA-CFAR Over the Signals $s_+(t)$ and $s_-(t)$ Reverted From SPWVD for AH-64 APACHE and EC-130

After finding the flash instances, the $T_{flash,approaching}$ and $T_{flash,receding}$ can be estimated as

$$T_{flash,approaching} = \frac{1}{N-1}\sum_{i=1}^{N-1}(t_{(i+1),(approaching)} - t_{(i),(approaching)}) \tag{4.18}$$

$$T_{flash,receding} = \frac{1}{N-1}\sum_{i=1}^{N-1}(t_{(i+1),(receding)} - t_{(i),(receding)}) \tag{4.19}$$

It is very obvious that the approaching and receding flash periods are equal to each other for a helicopter. Therefore, $T_{flash,approaching}$ and $T_{flash,receding}$ are expected to

be equal. We can call them T_{flash}. However, for more accurate evaluation of the period, the average of $T_{flash,approaching}$ and $T_{flash,receding}$ can be used as

$$T_{flash} = \frac{T_{flash,approaching} + T_{flash,approaching}}{2} \tag{4.20}$$

4.4.2 Finding Maximum Tip Doppler Frequency ($F_{D,tip}$)

To find the blade length, it is necessary to find the maximum tip Doppler frequency of the blade at flash instant. Figure 4.13 shows time-frequency distribution at detected flash instances. Figure 4.13a and Figure 4.13c shows approaching blade flashes for AH-64 and EC-130 respectively. As seen from the figures, the frequencies are positive. Figure 4.13b and Figure 4.13d shows receding blade flashes for negative frequencies.

By summing up energy distributions for all flashes (for approaching and receding blades separately), we will get the spectrum of blades at flash instances. This is equivalent to use the flash instances of time signal to get the spectrum. To find the maximum tip Doppler frequency ($F_{D,tip}$) of blades, edge detection algorithm is implemented. The edge detection algorithm takes derivative of the obtained flash spectrum and finds the absolute peak value of the derivative of the spectrum.

Figure 4.14 shows the spectrum of flashes and the derivative of it for the approaching and receding blades separately for AH-64 and EC-130. The blue line in the graphs shows the spectrum of flashes while the red line shows the derivative of the spectrum.

The absolute value of the detected tip Doppler frequency from the approaching and the receding blade return are expected to be equal. Because of this reason and for more accurate estimation, the maximum tip Doppler frequency ($F_{D,tip}$) can be estimated by averaging the calculated absolute values of tip Doppler frequencies for approaching and receding blade at flash instances.

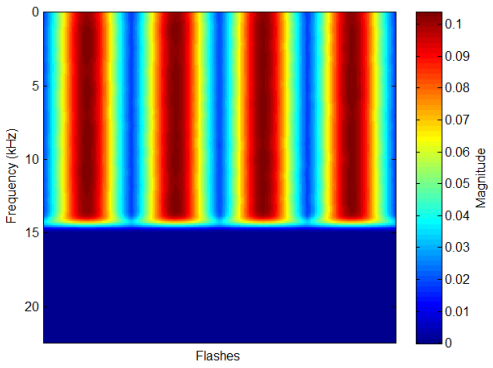

(a) Detected Approaching Flashes (AH-64 APACHE, 4.8 rps)

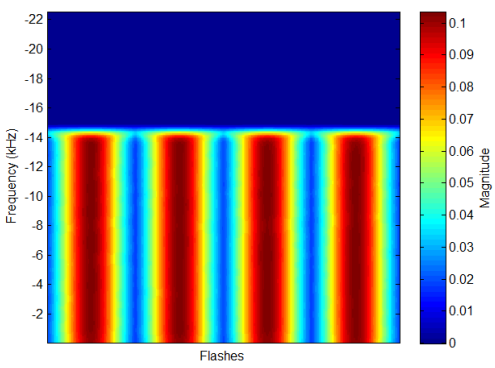

(b) Detected Receding Flashes (AH-64 APACHE, 4.8 rps)

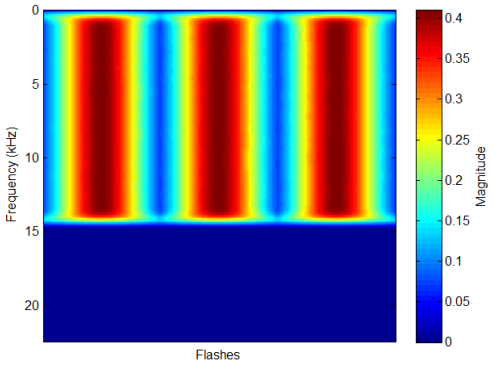

(c) Detected Approaching Flashes (EC-130, 6.5 rps)

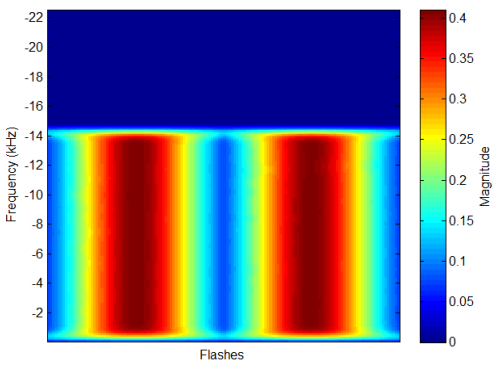

(d) Detected Receding Flashes (EC-130, 6.5 rps)

.

Figure 4.13: Detected Flashes in Frequency Domain for AH-64 APACHE and EC-130

In the spectrum of the blade returns given in Figure 4.4 and Figure 4.5, the maximum and the minimum frequency positions are determined by the blade tips. Therefore, the tip Doppler frequency can be measured from the spectrum of the return signal. However, knowing the flash instances is sufficient to determine maximum tip Doppler frequency. There is no need to use spectrum of entire time signal. Also, it is obvious that the spectrum of complete return signal is more noisy than the spectrum of only flashes. Therefore, estimating blade tip Doppler frequency from the spectrum of flashes yields more accurate results than the return signals spectrum.

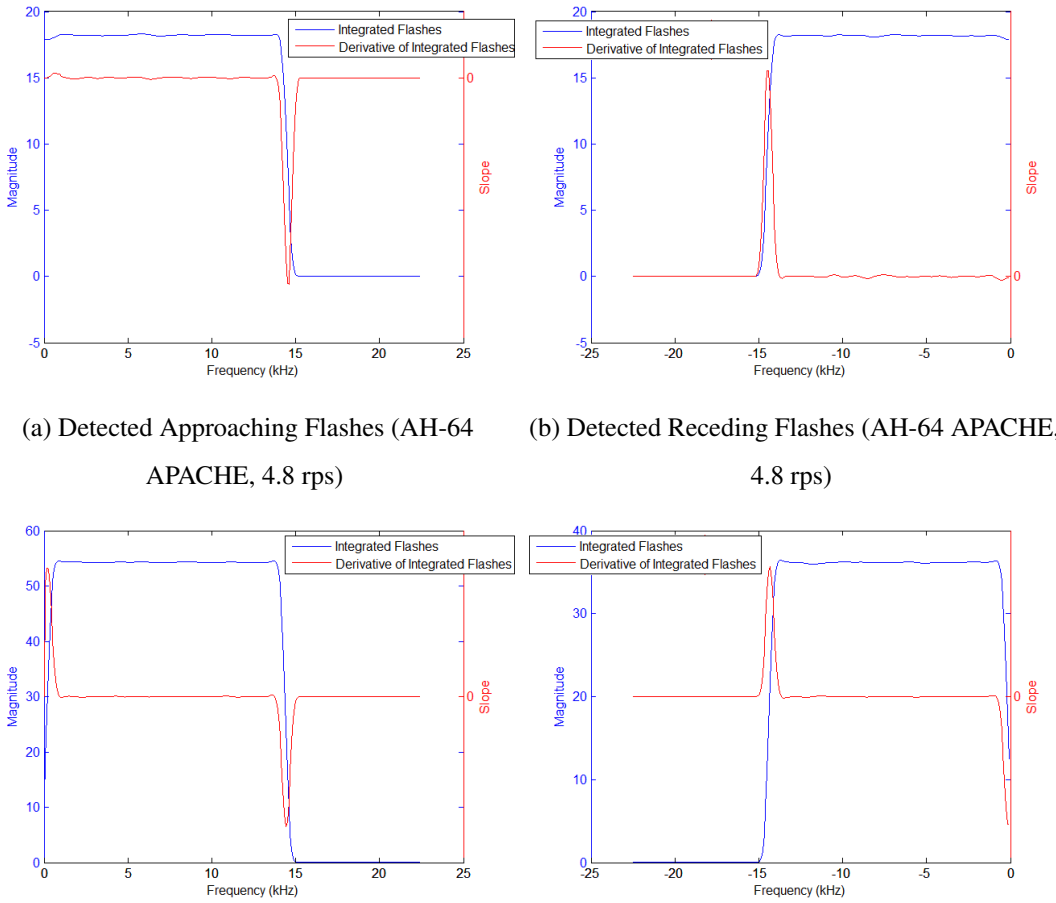

(a) Detected Approaching Flashes (AH-64 APACHE, 4.8 rps)

(b) Detected Receding Flashes (AH-64 APACHE, 4.8 rps)

(c) Detected Approaching Flashes (EC-130, 6.5 rps)

(d) Detected Receding Flashes (EC-130, 6.5 rps)

Figure 4.14: Detected Flashes in Frequency Domain for AH-64 APACHE and EC-130

4.4.3 Finding Tip Trace Period ($T_{\text{tip trace}}$)

For calculation of blade parameters, n and L, necessary parameters are T_{flash}, $F_{D,tip}$ and $T_{\text{tip trace}}$. In the previous sections, T_{flash} and $F_{D,tip}$ are extracted from the return signal. As seen from Equation 4.10 and Equation 4.11, $T_{\text{tip trace}}$ is necessary for calculation of both n and L. Remember that the definition of $T_{\text{tip trace}}$ is the period of the sinusoidal trace of blade tip in the time-frequency distribution.

Because the trace is a sinusoid, we can model it for one blade as

$$\text{tip trace} = A \times \cos(2\pi F_{\text{tip trace}} t + \phi_0) + B \tag{4.21}$$

where A is amplitude, B is dc level, $F_{\text{tip trace}}$ is frequency of the trace which is equal to $1/T_{\text{tip trace}}$ and the ϕ_0 is the initial phase of the sinusoidal trace.

Some of the tip trace parameters are already extracted in previous sections. It is obvious that the amplitude A of the sinusoidal trace is equal to $F_{D,tip}$. Because the radar compensates the velocity of the body of the helicopter, there is no dc level at the frequency. Therefore, B is equal to 0 . The constant phase term ϕ_0 is the phase of the cosine at $t = 0$. It corresponds to

$$\phi_0 = -2\pi F_{\text{tip trace}} t_f \tag{4.22}$$

where t_f is the first approaching flash instance of the corresponding blade. Therefore, the tip trace becomes

$$\text{tip trace} = F_{D,tip} \times \cos(2\pi \frac{1}{T_{\text{tip trace}}}(t - t_f)) \tag{4.23}$$

The only unknown parameter is the $1/T_{\text{tip trace}}$. Note that the trace periods of all blades are equal to each other for a helicopter because, as seen from Equation 4.9, it only depends on the f_{rotor} of the helicopter rotor. However, the boundaries of the $T_{\text{tip trace}}$ is not known. Because of these reasons, instead of searching the period of tip trace $T_{\text{tip trace}}$, it is better to search the blade number n. n can get a limited number of values, 2, 3, 4, 5, 6 or 7. Also as seen from Equation 4.10, the $T_{\text{tip trace}}$ in Equation 4.25 can be rewritten by using n as

$$T_{\text{tip trace}} = n \times T_{flash} \tag{4.24}$$

where T_{flash} is found in the previous section.

4.4.3.1 Estimation Of The Number Of Blades Using Hough Transform

Hough transform is a method for detecting complex patterns on a binary image [31] [30] [32] [34]. The Hough transform maps the features of an image into sets of points in the parameter space. The basic idea of the Hough transform is accumulating the values of the pixels through the created test lines. The test lines are created with the different parameters from the parameter set. At the end of the procedure, there will be a matrix called Hough matrix. The dimension of the Hough matrix is equal to the number of parameters used in Hough transform. The advantages of the Hough transform are its robustness to noise and discontinuities in the pattern [33]. The main disadvantage of the Hough transform is the necessary storage and the exponentially growing complexity of the algorithm when the number of searched parameters increase [30] [33].

Although the Hough transform is defined for binary images, it can used in gray scale images. Note that the time-frequency distribution can be treated as a gray scale image. In our case, the searched line is a sinusoid given in Equation 4.23. The only parameter for the Hough transform is the period of tip trace $T_{\text{tip trace}}$. Equation 4.23 is derived for the trace of one blade. For each blade of the helicopter, the tip traces are

$$\text{tip trace}_i = F_{D,tip} \times \cos(2\pi \frac{1}{n \times T_{flash}}(t - t_{f,i})) \tag{4.25}$$

where $t_{f,i}$ is the first approaching flash instance of the i^{th} blade. The $F_{D,tip}$, T_{flash} and flash instances ($t_{f,i}$) are found in previous sections. However, it is not possible to know which flash corresponds to which blade. The first approaching flash instance of each blade ($t_{f,i}$) can be found separately by using the first approaching flash instance of the first blade ($t_{f,1}$) and the T_{flash}. Remember that the definition of the T_{flash} is the flash period of approaching (and/or receding (they are equal)) blade flashes. It is obvious that the time between the approaching flash instances is equal to T_{flash}. Therefore, $t_{f,i}$ is

$$t_{f,i} = t_{f,1} + (i - 1) \times T_{flash} \tag{4.26}$$

where $t_{f,1}$ is the first approaching blade flash of first blade. The resultant trace for i^{th} blade for n blade helicopter is

$$\text{tip trace}_i = F_{D,tip} \times \cos(2\pi \frac{1}{n \times T_{flash}}(t - (t_{f,1} + (i-1) \times T_{flash}))) \qquad (4.27)$$

To increase the detection performance of Hough transform, a modification should be made on the time-frequency distribution. Remember that the basic idea behind the Hough transform is to accumulate the values of the pixels through the test lines. The value of the corresponding entry of the Hough matrix increases unnecessarily when the trace intersects with one of the blade flashes. The value of the pixels through the flash is very high compared to the values through the tip trace. Therefore, the detection probability of Hough transform decreases. Also, as seen from Figure 4.7, for odd number of blades, there is blade root trace. As seen from Figure 4.15, the pixels at the flash instances and those around zero Doppler are masked before implementation of Hough transform.

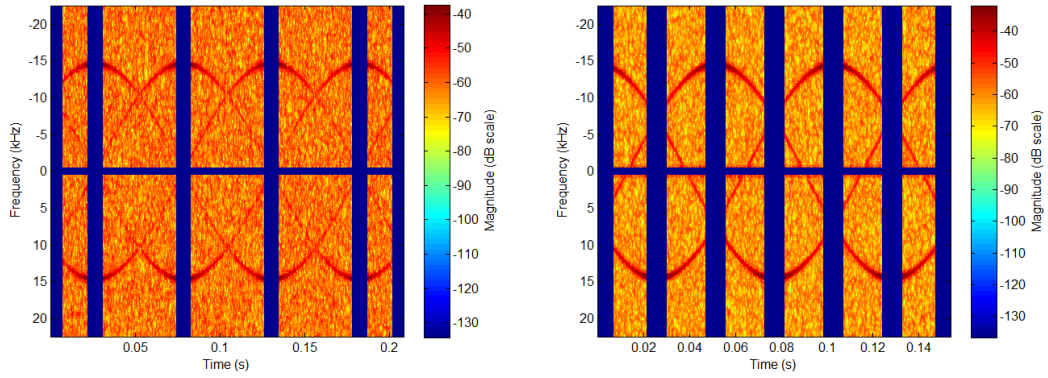

(a) Masked Time-Frequency Distribution for AH-64 APACHE, 4.8 rps

(b) Masked Time-Frequency Distribution for EC-130, 6.5 rps

Figure 4.15: Masked Time-Frequency Distributions for AH-64 APACHE and EC-130

For this case, the Hough matrix is one dimensional. The only searched parameter is the number of blades n.

However, the effectiveness of Hough transform is directly related with the accuracy of the estimated maximum tip Doppler frequency ($F_{D,tip}$). In case there is an inaccuracy

of the estimation of $F_{D,tip}$, it should be added to the search parameters. However, to decrease the computation time, the search boundaries for the tip Doppler frequency can be restricted with the calculated $\pm 3\%$. The value $\pm 3\%$ is found experimentally. Since it is already known whether the number of blades is even or odd, search parameters can further be reduced. If there are odd number of blades, the searched blade numbers are 3, 5 and 7, else the searched blade numbers are 2, 4 and 6.

Figure 4.16 shows the resultant Hough matrix for the time-frequency distribution images of the AH-64 APACHE and EC-130. As seen from the Hough matrix for AH-64 APACHE in Figure 4.16a, the maximum entry of the matrix is at 4 blade and 14.68 kHz. The Figure 4.16b shows the Hough matrix for EC-130. The maximum entry of the matrix is at 3 blade and 14.59 kHz. From Equation 4.10, the $T_{\text{tip trace}}$ can be calculated from the T_{flash} and n. The T_{flash} for the AH-64 APACHE has been calculated before and the number of blades is found by the Hough transform.

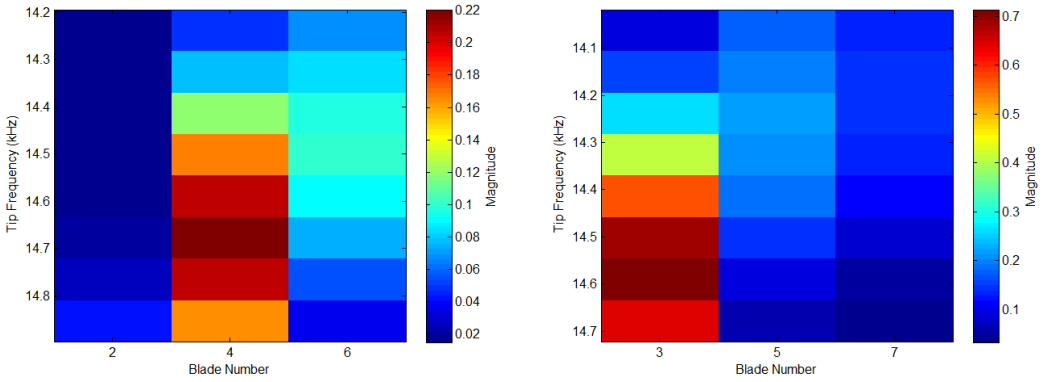

(a) Hough Matrix for AH-64 APACHE, 4.8 rps (b) Hough Matrix for EC-130, 6.5 rps

Figure 4.16: Hough Matrix for AH-64 APACHE and EC-130

4.5 Summary

For the classification of helicopters, required features are the number of blades n and the length of the blades L. Equation 4.10 and Equation 4.11 show how the blade features can be calculated from the extracted signal parameters. As seen from Equation 4.10 and Equation 4.11, the necessary parameters to calculate blade features are T_{flash}, $T_{\text{tip trace}}$ and $F_{D,tip}$. The T_{flash} was calculated by applying CA-CFAR algo-

rithm to the synthetic time signals reverted from the time-frequency distribution in Section 4.4.1. The $T_{\text{tip trace}}$ is obtained as an indirect result of the Hough transform in Section 4.4.3. The $F_{D,tip}$ is calculated using the flashes in the time-frequency distribution in Section 4.4.2. However, $F_{D,tip}$ is also searched with the Hough transform for fine-tuning in Section 4.4.3.

CHAPTER 5

SIMULATION RESULTS

In this chapter, the simulation results of the proposed algorithm for different type of helicopters, different time-frequency distribution techniques and with different SNR values will be given.

5.1 Simulation Configurations

Simulations are performed for each helicopter given in Table 5.1 for average SNR values of 30, 25, 20, 15, 10, 5, 0, -5 and -10 dB. Also, To get reliable results, each simulation is performed for 20 times. Note that the f_{rotor} values of the helicopters are chosen as the $0.7\times$ maximum rps values, which are close to their nominal operational values. To compare effectiveness of different time-frequency distributions for our proposal, all simulations are repeated for SPWVD, GDLD and CWD.

The blade return signal is modeled as if it obtained by a pulse-Doppler tracking radar with carrier frequency of 10 GHz and with constant prf of 90 kHz. The reason of choosing these parameters and the radar model are explained in the previous chapter. While sampling the blade dynamics with radar, the f_{rotor} values of the helicopter rotors are assumed to stay constant. The observation duration of the radar is assumed to be 0.5 seconds for all configurations, which corresponds to maximum of periods of the rotors of the helicopters given in Table 5.1 (Note that CH-53E has the maximum period, which is 0.493 seconds).

Average SNR is the most suitable choice for our situation because of the reasons given

Table 5.1: Simulated Helicopter Parameters

Helicopter	**Blade Length (m)**	**Number of Blades**	f_{rotor}
AH-1W	7.3	2	3.43
EC-130	5.35	3	4.55
AH-64	7.3	4	3.36
MD-500	4.02	5	5.74
CH-53	11	6	2.17
CH-53E	12.04	7	2.03

in previous chapter. The corresponding peak-SNR values of blade return signals are given in Table 5.2. As seen from the table, although average SNR values are the same, the PSNR values are different. This is because longer blade length will have a shorter duration while shorter blade will be splayed over time [24] and then the resultant peak powers are different.

Table 5.2: The PSNR Values Corresponding to Different Average SNR's of Used Helicopters

	AH-1W	**EC-130**	**AH-64**	**MD-500**	**CH-53**	**CH-53E**
-10 dB	25.4 dB	15.7 dB	21.7 dB	12.2 dB	21.5 dB	15.4 dB
-5 dB	30.4 dB	20.7 dB	26.6 dB	17.3 dB	26.5 dB	20.5 dB
0 dB	35.4 dB	25.7 dB	31.7 dB	22.3 dB	31.6 dB	25.5 dB
5 dB	40.4 dB	30.7 dB	36.6 dB	27.3 dB	36.5 dB	30.5 dB
10 dB	45.4 dB	35.7 dB	41.7 dB	32.3 dB	41.5 dB	35.5 dB
15 dB	50.4 dB	40.7 dB	46.6 dB	37.3 dB	46.5 dB	40.5 dB
20 dB	55.4 dB	45.8 dB	51.7 dB	42.3 dB	51.6 dB	45.5 dB
25 dB	60.4 dB	50.7 dB	56.7 dB	47.3 dB	56.6 dB	50.5 dB
30 dB	65.4 dB	55.7 dB	61.7 dB	52.3 dB	61.5 dB	55.5 dB

The results are obtained to measure performances of flash period (T_{flash}) estimator, maximum tip Doppler frequency ($F_{D,tip}$) estimator and number of blades (n) estimator. For flash period (T_{flash}) and maximum tip Doppler frequency ($F_{D,tip}$), the root mean square error (RMSE) is used as a measure. However, because the number of blades can take only restricted integer values, instead of using RMSE, probability of success is used.

5.2 Results

Table 5.3 shows the normalized root mean square errors of the estimated flash periods (T_{flash}). Remember that the T_{flash} is calculated by using the found flash time instances and flash instances are found by using the CA-CFAR detector. Therefore, the table shows the effectiveness of applying CA-CFAR detector algorithm to flash detection over time-frequency distribution. As seen, obtained RMSE values are negligibly small. For all cases, the RMSE value is decreasing from -10 to 0 dB. After that point, The RMSE value nearly stays constant while average SNR is increasing. As a result, all methods gives nearly the same performance for the estimation of T_{flash}. Note that the values on the table is expressed as a percentage of the actual flash period.

Table 5.3: Normalized RMSE Values of Estimated Flash Periods (T_{flash})

	SPWVD	**GDLD**	**CWD**
-10 dB	%0.795785	%0.694398	%0.755054
-5 dB	%0.040620	%0.042620	%0.036620
0 dB	%0.000683	%0.000658	%0.000684
5 dB	%0.000657	%0.000635	%0.000623
10 dB	%0.000650	%0.000675	%0.000537
15 dB	%0.000607	%0.000620	%0.000542
20 dB	%0.000603	%0.000620	%0.000527
25 dB	%0.000610	%0.000603	%0.000520
30 dB	%0.000604	%0.000570	%0.000358

Table 5.4 shows the RMSE values of the estimated maximum tip Doppler frequency ($F_{D,tip}$). The maximum tip Doppler frequency is extracted by using the spectrum of flashes obtained from the flash times. For SPWVD case, the RMSE values are below the %1 which means that the standard deviation of the error is below the %0.5 of the actual maximum tip Doppler frequency. For the GDLD case, the RMSE is just above %1 and for CWD case, it is just below the %1. For all cases, the effect of SNR is small. As a result, SPWVD and CWD methods gives nearly the same performance for the estimation of $F_{D,tip}$ and they are better than the GDLD method. Note that the values on the table is expressed as a percentage of the actual tip Doppler frequency.

Figure 5.1 shows the probability of successful estimation of number of blades versus average SNR for different helicopters and for different time-frequency distributions.

Table 5.4: Normalized RMSE Values of Estimated Tip Doppler Frequency ($F_{D,tip}$)

	SPWVD	**GDLD**	**CWD**
-10 dB	%0.898569	%1.083545	%0.884094
-5 dB	%0.885258	%1.072466	%0.869259
0 dB	%0.868521	%1.066753	%0.855594
5 dB	%0.842364	%1.066547	%0.830107
10 dB	%0.855791	%1.054782	%0.826614
15 dB	%0.831215	%1.036541	%0.827515
20 dB	%0.821547	%1.011862	%0.823254
25 dB	%0.833254	%1.018625	%0.821456
30 dB	%0.828014	%1.010547	%0.823354

The blue lines show SPWVD, red lines show GDLD and the green line show CWD method.

Figure 5.1a shows the success probability for AH-1W. For SPWVD method, for 15 dB and higher average SNR values, the success probability is nearly 100%. For GDLD method, the probability of success is nearly 100% for 25 dB or higher average SNR. For CWD method, up to 20 dB average SNR, the probability of success is nearly 100%.

Figure 5.1b shows the success probability for EC-130. For SPWVD method, for 10 dB and higher average SNR values, the success probability is nearly 100%. For GDLD method, the probability of success is nearly 100% for 20 dB and higher average SNR values. For CWD method, up to 15 dB average SNR, the probability of success is nearly 100%.

Figure 5.1c shows the success probability for AH-64. For SPWVD method, for 10 dB and higher average SNR values, the success probability is nearly 100%. For GDLD and CWD methods, the probability of success is nearly 100% for 20 dB and higher average SNR.

Figure 5.1d shows the success probability for MD-500. For SPWVD and CWD method, for 15 dB and higher average SNR values, the success probability is nearly 100%. For GDLD method, the probability of success is nearly 100% for 20 dB and higher average SNR.

Figure 5.1e shows the success probability for CH-53. For All methods, for 20 dB and higher SNR values, the probability of success is nearly 100%.

Figure 5.1f shows the success probability for CH-53E. For All methods, for 20 dB and higher SNR values, the probability of success is nearly 100%.

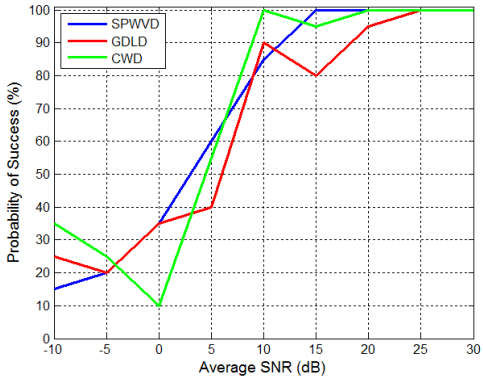

(a) AH-1W.

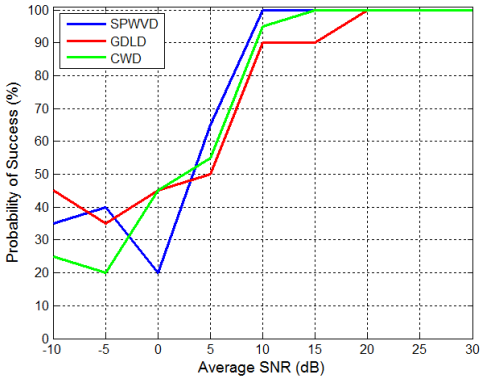

(b) EC-130.

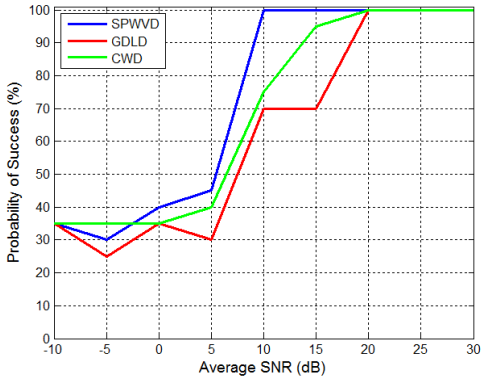

(c) AH-64.

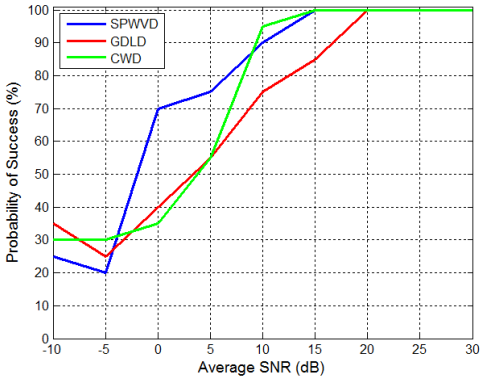

(d) MD-500.

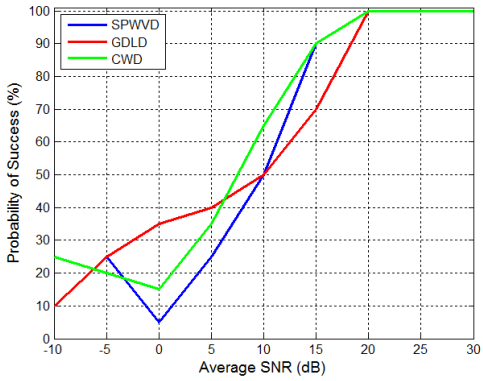

(e) CH-53.

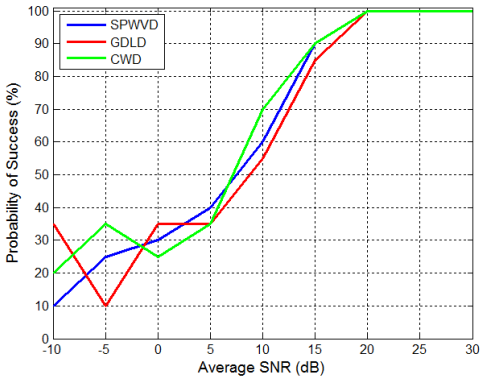

(f) CH-53E.

Figure 5.1: Probability of Successful Estimation of Number of Blades versus Average SNR For Different Type of Helicopters.

All the graphs in Figure 5.1 shows that, from an SNR point, the probability of successful estimation of number of blades decreases with the decreasing average SNR as expected.

Figure 5.2 shows an average value for the probability of successful estimations of number of blades. This graph is obtained by averaging the values given in Figure 5.1. As seen from the figure, down to 20 dB average SNR, the probability of success is same for all of the three methods. However, after that point, the probability obtained with the GDLD method decreases sharper than the others while SPWVD and CWD methods show nearly same characteristic.

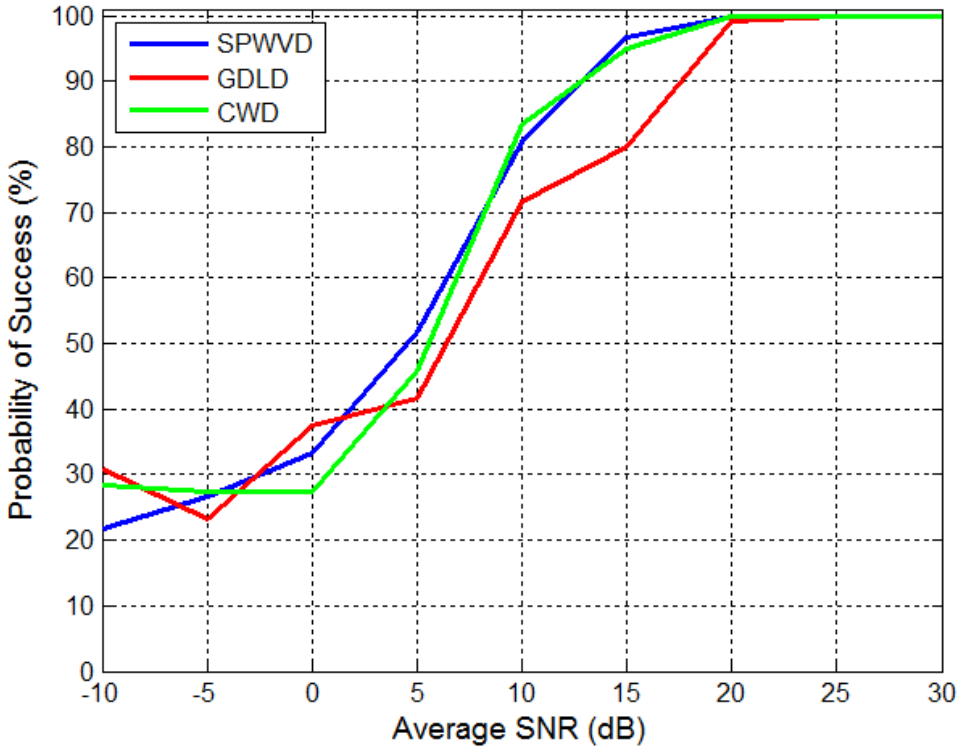

Figure 5.2: Average Probability of Successful Estimation of Number of Blades versus Average SNR

Figure 5.3 shows the time costs of the time-frequency distribution methods. Note that the values are normalized to the time cost of GDLD, such that its cost is equal to 1. As seen from the figure, costs of SPWVD and the CWD is nearly the cost of GDLD is higher than them.

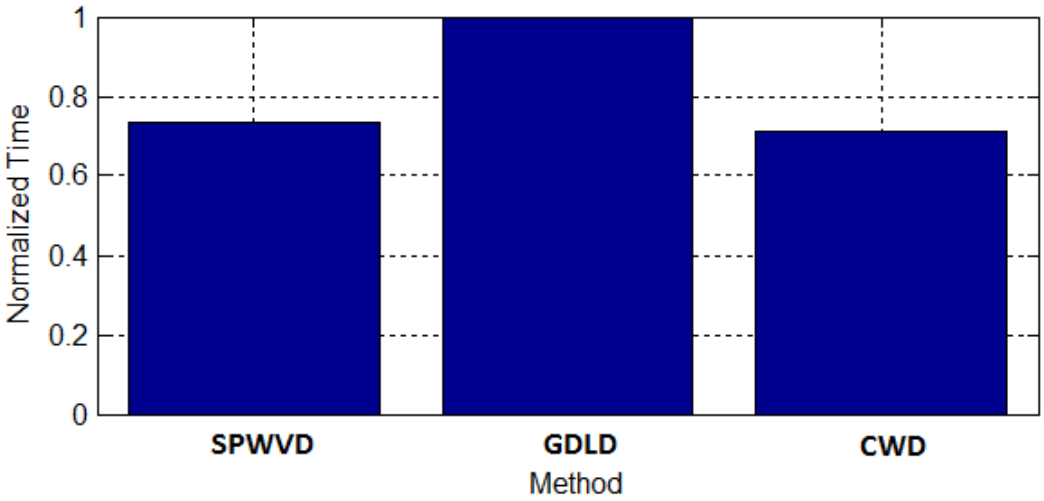

Figure 5.3: Time Costs of Time-Frequency Transform Methods

The results show that while our algorithm estimates the $F_{D,tip}$ and the T_{flash} well even for lower average SNR values like -10 dB, the estimation of number of blades requires high average SNR values such as 20 dB and higher. This is because, to estimate the $F_{D,tip}$ and the T_{flash}, the blade flashes are used and the RCS of the blade is maximum at the flash instant. However, to estimate the number of blades, trace of blade tip is used. If one wants to classify helicopters by L / n quotient, without finding the blade parameters unambiguously, the proposed technique without Hough transform offers high probability of success even for low SNR values.

CHAPTER 6

CONCLUSIONS AND FUTURE WORK

In this work, we introduced a procedure for micro-Doppler analysis of helicopter return signal in order to extract the blade parameters. The proposed method combines both time-frequency analysis and Hough transform . From the micro-Doppler signatures of the return signal, we calculated the blade parameters which are number of blades, blade length an angular velocity. We also compare the effectiveness of different bilinear time-frequency techniques for our algorithm.

To process micro-Doppler signatures of blades, firstly we obtained the time-frequency distribution. Instead of using short time Fourier transform, we used bilinear time-frequency distribution techniques, since bilinear transforms offer more resolution in both time and frequency. After getting the distribution, we obtained the separate flash instances of approaching and receding blades by using CA-CFAR detector. With the obtained flash instances, we calculated the period of approaching and receding blade flashes. Then, we obtain the maximum tip Doppler frequency, which occurs when blade is perpendicular to radar line of sight. We used Fourier transform of blade return signal to extract this information. However, to increase SNR value, we used small time windows near flash instances to get Fourier transform. However, period of flashes and maximum tip Doppler frequency does not give the blade parameters without the f_{rotor} estimate unambiguously. Because of this reason, to extract the f_{rotor} of the rotor, we applied the Hough transform to the time-frequency distribution image with the extracted parameters.

Simulation results show that our algorithm is very effective under certain conditions. As seen from Figure 5.2, Table 5.3 and Table 5.4, for 20 dB and higher average SNR

values, the probability of success of our algorithm is nearly 100% and the error ratio is below %1. We also conclude that the Hough transform can be applied on the time-frequency distributions to recognize expected patterns. Another result of our work is that the SPWDV and CWD give nearly the same results. And they performs better than the GDL for our algorithm. Also the cost of SPWVD and the CWD is less then the GDLD. In addition, this work shows that it is feasible to use CA-CFAR for the purpose of finding flash instances.

For future work, some of the issues that may be explored are listed below:

- expanding the algorithm for jet engine parameter extraction,
- analysis of helicopters that have double main rotor, such as *CH-47 Chinook*,
- analysis of tail rotor return signal,
- estimation of blade parameters using bi-static radar,
- analysis of real helicopter signal and comparison of the results with synthetic signal results,
- design of a new kernel for Cohen's class distribution to analyze blade signals.

REFERENCES

[1] Temes, Clifford L. "Relativistic Consideration of Doppler Shift." Aeronautical and Navigational Electronics, IRE Transactions on 1 (1959): 37-37.

[2] Richards, Mark A. Fundamentals of radar signal processing. Tata McGraw-Hill Education, 2005.

[3] Melino, R., C. Bourne, and H. T. Tran. Modelling Helicopter Radar Backscatter. No. DSTO-TR-2547. Defence Science and Technology Organisation Edinburgh (Australia) Electronic Warfare and Radar Division, 2011.

[4] Cilliers, A., and W. A. J. Nel. "Helicopter parameter extraction using joint time-frequency and tomographic techniques." Radar, 2008 International Conference on. IEEE, 2008.

[5] Chen, Victor. The micro-Doppler effect in radar. Artech House, 2011.

[6] Cohen, Leon. Time-frequency analysis: theory and applications. Prentice-Hall, Inc., 1995.

[7] Chen, Victor C., et al. "Micro-Doppler effect in radar: phenomenon, model, and simulation study." Aerospace and Electronic Systems, IEEE Transactions on 42.1 (2006): 2-21.

[8] Chen, Victor C., et al. "Analysis of micro-Doppler signatures." IEE Proceedings-Radar, Sonar and Navigation 150.4 (2003): 271-276.

[9] Thayaparan, Thayananthan, et al. "Analysis of radar micro-Doppler signatures from experimental helicopter and human data." IET Radar, Sonar & Navigation 1.4 (2007): 289-299.

[10] Cohen, Leon. "Time-frequency distributions-a review." Proceedings of the IEEE 77.7 (1989): 941-981.

[11] Lağoğlu, Berker. Performance of bilinear time-frequency transforms in isar. Diss. Middle East Technical University, 2007.

[12] Cohen, Leon. "Generalized phase-space distribution functions." Journal of Mathematical Physics 7.5 (2005): 781-786.

[13] Thayaparan, T., and S. Kennedy. "Detection of a manoeuvring air target in sea-clutter using joint time-frequency analysis techniques." Radar, Sonar and Navigation, IEE Proceedings-. Vol. 151. No. 1. IET, 2004.

[14] Wigner, Eugene. "On the quantum correction for thermodynamic equilibrium." Physical Review 40.5 (1932): 749.

[15] Ville, J. de. "Théorie et applications de la notion de signal analytique." Cables et transmission 2.1 (1948): 61-74.

[16] Jeong, Jechang, and William J. Williams. "Kernel design for reduced interference distributions." Signal Processing, IEEE Transactions on 40.2 (1992): 402-412.

[17] Hlawatsch, Franz. "Interference terms in the Wigner distribution." Digital Signal Processing 84 (1984): 363-367.

[18] Qian, Shie, and Dapang Chen. "Decomposition of the Wigner-Ville distribution and time-frequency distribution series." Signal Processing, IEEE Transactions on 42.10 (1994): 2836-2842.

[19] Claasen, T. A. C. M., and W. F. G. Mecklenbrauker. "The Wigner distribution—A tool for time-frequency signal analysis." Part I-III, Philips J. Res 35.3 (1980): 217-250.

[20] Hlawatsch, Franz, et al. "Smoothed pseudo-Wigner distribution, Choi-Williams distribution, and cone-kernel representation: Ambiguity-domain analysis and experimental comparison." Signal Processing 43.2 (1995): 149-168.

[21] Hlawatsch, Franz, and G. Faye Boudreaux-Bartels. "Linear and quadratic time-frequency signal representations." IEEE Signal Processing Magazine 9.2 (1992): 21-67.

[22] Choi, H-I., and William J. Williams. "Improved time-frequency representation of multicomponent signals using exponential kernels." Acoustics, Speech and Signal Processing, IEEE Transactions on 37.6 (1989): 862-871.

[23] Guo, Zhenyu, L-G. Durand, and Howard C. Lee. "The time-frequency distributions of nonstationary signals based on a Bessel kernel." Signal Processing, IEEE Transactions on 42.7 (1994): 1700-1707.

[24] Chen, Victor C., and Hao Ling. Time-frequency transforms for radar imaging and signal analysis. Artech House, 2002.

[25] Tait, Peter. Introduction to radar target recognition. Vol. 18. IET, 2005.

[26] Gandhi, Prashant P., and Saleem A. Kassam. "Analysis of CFAR processors in homogeneous background." Aerospace and Electronic Systems, IEEE Transactions on vol. 24, no. 4 (1988): 427-445.

[27] Guo, Zhenyu, L-G. Durand, and Howard C. Lee. "Comparison of time-frequency distribution techniques for analysis of simulated Doppler ultrasound

signals of the femoral artery." Biomedical Engineering, IEEE Transactions on 41.4 (1994): 332-342.

[28] Papandreou, Antonia, and G. Faye Boudreaux-Bartels. "Distributions for time-frequency analysis: a generalization of Choi-Williams and the Butterworth distribution." Acoustics, Speech, and Signal Processing, 1992. ICASSP-92., 1992 IEEE International Conference on. Vol. 5. IEEE, 1992.

[29] Mahafza, Bassem R. Radar signal analysis and processing using MATLAB. CRC Press, 2008.

[30] Illingworth, John, and Josef Kittler. "A survey of the Hough transform." Computer vision, graphics, and image processing 44.1 (1988): 87-116.

[31] Hough, Paul VC. "Method and means for recognizing complex patterns." U.S. Patent No. 3,069,654. 18 Dec. 1962.

[32] Ballard, Dana H. "Generalizing the Hough transform to detect arbitrary shapes." Pattern recognition 13.2 (1981): 111-122.

[33] Changchun, Zou, and Shi Ge. "A Hough transform-based method for fast detection of fixed period sinusoidal curves in images." Signal Processing, 2002 6th International Conference on. Vol. 1. IEEE, 2002.

[34] Duda, Richard O., and Peter E. Hart. "Use of the Hough transformation to detect lines and curves in pictures." Communications of the ACM 15.1 (1972): 11-15.

[35] O'shea, Peter. "A new technique for instantaneous frequency rate estimation." Signal Processing Letters, IEEE 9.8 (2002): 251-252.

[36] O'Shea, Peter. "A fast algorithm for estimating the parameters of a quadratic FM signal." Signal Processing, IEEE Transactions on 52.2 (2004): 385-393.

[37] Wang, Pu, et al. "Integrated cubic phase function for linear FM signal analysis." Aerospace and Electronic Systems, IEEE Transactions on 46.3 (2010): 963-977.

[38] Li, Po, De-Chun Wang, and Jin-Li Chen. "Parameter estimation for micro-Doppler signals based on cubic phase function." Signal, Image and Video Processing 7.6 (2013): 1239-1249.

[39] Wang, Pu, and Jianyu Yang. "Multicomponent chirp signals analysis using product cubic phase function." Digital Signal Processing 16.6 (2006): 654-669.

[40] Setlur, Pawan, Fauzia Ahmad, and Moeness Amin. "Helicopter radar return analysis: Estimation and blade number selection." Signal Processing 91.6 (2011): 1409-1424.

[41] Rotander, C. E., and H. Von Sydow. "Classification of helicopters by the L/N-quoutient." (1997): 629-633.

[42] Yoon, Sang-Ho, Byungwook Kim, and Young-Soo Kim. "Helicopter classification using time-frequency analysis." Electronics Letters 36.22 (2000): 1871-1872.